IEEE Access
Multidisciplinary | Rapid Review | Open Access Journal

Received 8 September 2023, accepted 9 October 2023, date of publication 19 October 2023, date of current version 25 October 2023.

Digital Object Identifier 10.1109/ACCESS.2023.3325995

RESEARCH ARTICLE

Novel Movement-Based Methods for the Calibration of Colocated Multiple-Input Multiple-Output Radars

GIORGIO GUERZONI[1], ELAHE FAGHAND[1,2], GIORGIO MATTEO VITETTA[1], (Senior Member, IEEE), LORIS VINCENZI[1], AND ESFANDIAR MEHRSHAHI[2]

[1]Department of Engineering "Enzo Ferrari", University of Modena and Reggio Emilia, 41124 Modena, Italy
[2]Department of Telecommunications, Faculty of Electrical Engineering, Shahid Beheshti University, Tehran 19839 69411, Iran

Corresponding author: Giorgio Guerzoni (giorgio.guerzoni@unimore.it)

This work was supported by the Department of Engineering "Enzo Ferrari" through the research project "MIMO radar for Structural Health Monitoring" under Grant FARD2022.

ABSTRACT It is well-known that the availability of transmit and receive arrays in colocated multiple-input multiple-output radar systems can be exploited to detect multiple targets, and estimate their range and angular coordinates. Unluckily, the accuracy achieved in the estimation of target parameters can be severely affected by hardware nonidealities. The impact of these nonidealities can be mitigated through the adoption of specific methods explicitly developed to estimate and compensate for them, i.e., briefly, of calibration methods. As far as we know, until now, most of the calibration techniques proposed in the technical literature for colocated multiple-input multiple-output radars are based on the idea of placing one or more reference targets in front of the considered radar device at perfectly known and fixed locations, and quantifying the difference between the expected radar image and the measured one. In this manuscript, two novel calibration methods are proposed. Both exploit the measurements captured by a colocated multiple-input multiple-output radar device at multiple positions; for this reason, the acquisition of such measurements involves the movement of the radar. The first one does not require any knowledge about the nature, number, position or radar cross section of the reference targets, provided that all these are in far-field; the second one, instead, needs a single reference target in near-field conditions, with the only constraints for it to be pointwise and isolated from stray targets in the range domain. This drastically simplifies the experimental setup to be employed for radar calibration. The proposed methods are tested on a commercial radar device and compared with a traditional method for radar calibration.

INDEX TERMS Calibration, multiple-input multiple-output, radar, synthetic aperture radar.

I. INTRODUCTION

In the last few years, an increasing attention has been paid by a number of researchers to colocated *multiple-input multiple-output* (MIMO) radars because of their potential applications in a number of fields. These devices, being equipped with *transmit* (TX) and *receive* (RX) antenna arrays, can detect multiple targets and, unlike their *single-input single-output* (SISO) counterparts, are able to measure not only their range, but also their angular coordinates (namely, their azimuth and elevation); such coordinates are estimated by assessing the *angle-of-arrival* (AoA) of the electromagnetic echoes that originate from the detected targets [1]. In commercially available colocated MIMO radars, the accuracy of AoA estimation is influenced by *hardware nonidealities*, that can make the structure of the acquired measurements significantly different from that described by standard mathematical models (e.g., see [2], [3]). Well-known nonidealities in the considered radar systems include: a) *array shape* and *antenna misplacements*, that lead to an AoA-dependent phase error in the received signal; b) mismatches in the distribution and in the length of antenna feed lines, and tolerances in

The associate editor coordinating the review of this manuscript and approving it for publication was Xuebo Zhang.

TABLE 1. List of the manuscripts describing calibration methods based on the acquisition of measurements in a controlled propagation environment; the nonidealities to be compensated for are specified for each manuscript and for the two versions of the calibration method proposed in this manuscript (one requiring the acquisition of measurements in near-field conditions, the other one in far-field conditions; see the last two rows).

Work	Nonidealities			
	Phase	Frequency	RX-RX coupling	Array shape
Yanik & al. [4]	✓	✓	-	-
Rockah & al., I [5]	-	-	-	✓
Rockah & al., II [6]	-	-	-	✓
Weiss & al. [7]	-	-	-	✓
Schmid & al. [8]	✓	-	✓	-
Petrov & al. [9]	✓	-	✓	-
Durr & al. [10], [11]	-	-	-	✓
Geiss & al. [12]	✓	-	✓	-
Belfiori & al. [13]	✓	-	-	-
Tian & al. [14]	✓	-	-	-
Poh & al. [15]	✓	-	-	-
Proposed method, near-field	✓	✓	-	-
Proposed method, far-field	✓	✓	-	-

hardware components, both introducing phase and frequency offsets independent of AoA; c) TX-to-RX *coupling*, that generates strong low frequency components in the baseband received signal; d) RX-to-RX *coupling*, that, being angle-dependent, affects AoA estimation accuracy. The impact of these nonidealities on radar performance can be mitigated by estimating the resulting signal distortions and compensating for them (when possible), i.e., briefly, by accomplishing radar *calibration* on the basis of a set of measurements acquired in a controlled propagation environment; this allows to reduce the difference between the behaviour of real hardware and that described by standard mathematical models, so improving the reliability of acquired measurements [16].

In principle, full calibration would require accomplishing the following three tasks[1]:

1) Deleting the low frequency components due to TX-to-RX coupling; this result can be obtained by subtracting the time domain deterministic coupling signal (provided that this is known) or by inserting an high-pass filter at the output of the downconversion mixers at the RX side.

2) Applying proper phase and frequency shifts to the signals provided by the available virtual channels in order to align their spectra [17], [18].

3) Multiplying the RX signal matrix by the inverse of the RX-RX coupling matrix [19]. Note that, in principle, one matrix would be required for each AoA; however, in practice, a single coupling matrix can be used for the full field of view with good results [20], [21].

The calibration of colocated MIMO radars in a controlled propagation environment has been investigated in a limited number of technical manuscripts. A list of such manuscripts is provided in Table 1, where the nonidealities for which the proposed calibration methods have been developed are specified. Note that these methods may also differ for the experimental setup employed in the acquisition of the measurements they process. In fact, they may need: a) the knowledge of the position and/or the number of the employed reference targets; b) the positioning of the reference targets in near-field or far-field; c) the availability of an anechoic chamber or a controlled (e.g., multipath-free) environment whose size depends on the radar aperture if far-field conditions are required. A list of the requirements of the experimental setups described in the references of Table 1 is provided in Table 2. It is also worth mentioning that some calibration methods developed to compensate for the coupling and the phase mismatches of radars already mounted in their final position (e.g., on a vehicle) have been also devised [19], [22], [23]. Such methods do not require a specific experimental setup, and are based on tracking radar movement via a Kalman filter [22] or a MUSIC-like eigendecomposition [19], or on evaluating the mutual coupling between antennas [24] or on maximising the contrast of radar images [23].

The most critical issue in the use of the above mentioned calibration methods undoubtedly concerns the needed experimental setup. As it can be easily inferred from Table 2, the calibration methods illustrated in [4], [5], [7], [8], [13], and [22] require the use of an anechoic chamber containing one or more reference targets; these are placed in the far-field region of the device under test at precisely known locations. Since all this is costly and time-consuming, various efforts have been made to develop alternative methods relying on substantially simpler setups [6], [10], [12]. Another relevant technical issue

[1]Note that the most important of these steps is the second one, whereas the less important is the last one.

TABLE 2. Requirements of the experimental setup adopted for radar calibration in the manuscripts listed in Table 1.

Work	Requirements			
	Target position	Number of targets	Anechoic chamber or another controlled environment	Far-field
Yanik & al. [4]	Y	Y	Large	Y
Rockah & al., I [5]	-	Y	Large	Y
Rockah & al., II [6]	-	Y	Large	-
Weiss & al [7]	-	Y	Large	Y
Schmid & al. [8]	Partially	Y	Large	Y
Petrov & al. [9]	Partially	Y	Large	Y
Durr & al. [10], [11]	Y	Y	Small	-
Geiss & al. [12]	-	Y	Small	-
Belfiori & al. [13]	-	Y	Large	Y
Tian & al. [14]	Y	Y	None	Y
Poh & al. [15]	Y	Y	Large	Y
Proposed method, near-field	**-**	**Y**	**Small**	**-**
Proposed method, far-field	**-**	**-**	**None**	**Y**

is represented by the size of the propagation environment in which the measurements required for radar calibration need to be acquired. In fact, if such measurements can be obtained in near-field conditions, the overall calibration procedure involves a restricted area and, consequently, becomes simpler.

In this manuscript, the problem of compensating for phase and frequency mismatches in the TX and RX arrays of a colocated MIMO radar is tackled and a novel solution is developed. The proposed solution is based on the idea that, in principle, the signals captured by two distinct RX antennas belonging to the same radar device and placed exactly in the same position at different times should be identical if the employed TX antenna, the waveform radiated by it and the surrounding propagation scenario do not change. Therefore, any difference in the phase/frequency of the downconverted signals received through the considered couple of RX antennas can only originate from hardware nonidealities and can be exploited to estimate them. All this can be elegantly reformulated for a colocated MIMO radar system since, under certain conditions, any couple of its distinct TX and RX antennas can be approximated by *a single antenna of a virtual monostatic radar*, i.e., briefly, by a *virtual antenna* (VA). In fact, based on our previous considerations, we can state that, if distinct VAs are positioned at exactly the same point, the measurements provided by them should be identical in the absence of noise and nonidealities. In practice, these measurements can be acquired by installing the radar to be calibrated on an actuator that allows to move it with high spatial accuracy and without changing its orientation. In fact, if the geometry of the TX and RX arrays of the considered radar is perfectly known, its distinct VAs can be positioned at exactly the same point sequentially by simply moving this device. To the author's knowledge, this approach to radar calibration has never been proposed in the technical literature. Moreover, the calibration method based on it and called *Movement-Based Calibration* (MBC), if employed in *far-field* conditions, offers the following advantages with respect to the currently available alternatives:

a) It is *unaffected* by multipath.

b) It does not require any pointwise reference target; extended targets are suited as well.

c) It does not need any prior knowledge or setting specific constraints on the propagation environment.

d) It requires radar displacements smaller than those needed by other calibration methods.

Consequently, MBC can be used in a *completely uncontrolled* far-field environment; this means that there is no need to employ reference targets or to remove undesired objects potentially affecting other calibration methods [14], [25], [26].

Another relevant feature of the MBC approach is represented by the fact that it can be used in *near-field* conditions as well, albeit with some modifications. In this case, the main issue is not represented by the need of taking into account wavefront curvature and range/angle coupling phenomena [11] (to which our approach is insensitive), but from the fact that the VA approximation adopted in far-field conditions is no longer valid. In our work, this problem is circumvented by positioning a single pointwise target in the proximity of the considered radar and accurately estimating its coordinates; the last result is obtained through the exploitation of a *synthetic aperture*, which is generated by moving a single TX-RX couple.

In this manuscript, we concentrate on the application of MBC to a MIMO *frequency modulated continuous wave* (FMCW) radar; however, our method can be

easily reformulated for MIMO radars employing different waveforms.

The remaining part of this manuscript is organized as follows. The adopted system model is described in Section II, where the origin of the considered nonidealities is also illustrated. In Section III a well-known approach to radar calibration (dubbed *traditional calibration*, TC) is described, whereas our movement-based approach to radar calibration is developed for both far-field and near-field use conditions in Section IV. The impact of TC and MBC methods is analyzed in Section V. Finally, some conclusions are offered in Section VI.

II. SIGNAL AND SYSTEM MODELS

In this section, the architecture of the MIMO FMCW radar system considered in the remaining part of this manuscript is described. This radar system has the following essential features: a) it is equipped with TX and RX antenna arrays, consisting of N_T and N_R elements, respectively; b) the waveform radiated by each of its TX antennas (and generated by a *voltage controlled oscillator*, VCO) is a frequency modulated signal whose frequency increases linearly with time (i.e., a *chirp*); c) the architecture of its signal chain for an arbitrary couple of TX/RX antennas is described by the block diagram illustrated in Fig. 1, and referring to the lth TX antenna and the mth RX antenna (with $l = 1, 2, \ldots, N_T$ and $m = 1, 2, \ldots, N_R$). Note that this diagram allows us not only to describe the entire signal flow in the radar system, but also to highlight all the relevant delays characterizing the considered signal chain. Since these delays are *antenna dependent* (i.e., depend on l or/and m), they represent a source of *nonideality* to be compensated for through radar calibration. In the following, we illustrate the impact of such delays on the transmitted and received waveforms, and explain how target estimation is affected by them. In our analysis, we assume that the electromagnetic echo captured by the mth RX antenna originates from a single point-wise target;[2] this is placed at a distance R from the radar and its position is described by the coordinate vector $\mathbf{o} \triangleq (o_x, o_y, o_z)$, which is evaluated with respect to a *three-dimensional* (3D) reference system $\mathcal{O}$, solidal to the radar.[3] Moreover, we neglect, for simplicity, the effects of channel noise and of the attenuation due to propagation, waveguide absorption as well as gain mismatches, because all these have usually a smaller impact on target estimation than phase errors [27].

Our analysis starts from the TX side of the radar system shown in Fig. 1. The radar transmitter employs a VCO to generate the *radio frequency* (RF) waveform

$$s_I^{(\mathrm{VCO})}(t) \triangleq \cos\left(2\pi\left(f_0 + \mu t\right) t\right) \tag{1}$$

and its phase shifted version

$$s_Q^{(\mathrm{VCO})}(t) \triangleq -\sin\left(2\pi\left(f_0 + \mu t\right) t\right) \tag{2}$$

for $t \in [0, T)$; here, f_0 denotes the *start frequency* of the chirp, μ its *slope* and T its *duration*. The VCO signal $s_I^{(\mathrm{VCO})}(t)$ (1) travels, through a transmission line (usually a microstrip), to the lth TX antenna and to a downconversion mixer, whereas $s_Q^{(\mathrm{VCO})}(t)$ (2) feeds a different downconversion mixer (see Fig. 1). Therefore, the signal radiated by the lth TX antenna can be expressed as

$$s_l^{(\mathrm{TX})}(t) \triangleq s_I^{(\mathrm{VCO})}\left(t - \tau_l^{(\mathrm{TX})}\right), \tag{3}$$

where $\tau_l^{(\mathrm{TX})}$ denotes the (antenna dependent) delay due to the transmission line connecting the antenna itself to the VCO.

The signal $s_l^{(\mathrm{TX})}(t)$ (3) is reflected by a single point-wise target. The (antenna dependent) time intervals that this signal takes to travel from the lth TX antenna to the target and from the target to the mth RX antenna can be expressed as

$$\tau_l^{(\mathrm{F})} = \frac{1}{c}\left\|\mathbf{o} - \mathbf{p}_l^{(\mathrm{TX})}\right\|_2 \tag{4}$$

and

$$\tau_m^{(\mathrm{B})} = \frac{1}{c}\left\|\mathbf{o} - \mathbf{p}_m^{(\mathrm{RX})}\right\|_2, \tag{5}$$

respectively; here, $\|\cdot\|_2$ denotes the Euclidean norm and

$$\mathbf{p}_k^{(\mathrm{Z})} \triangleq \left(x_k^{(\mathrm{Z})}, y_k^{(\mathrm{Z})}, z_k^{(\mathrm{Z})}\right) \tag{6}$$

is the coordinate vector of the kth TX (RX) antenna if $\mathrm{Z} = \mathrm{TX}$ ($\mathrm{Z} = \mathrm{RX}$). Then, the signal available at the output of the mth RX antenna can be expressed as

$$\begin{aligned} s_{l,m}^{(\mathrm{RX})}(t) &\triangleq s_l^{(\mathrm{TX})}\left(t - \tau_{l,m}^{(\mathrm{RT})}\right) = \\ &= s_I^{(\mathrm{VCO})}\left(t - \tau_l^{(\mathrm{TX})} - \tau_{l,m}^{(\mathrm{RT})}\right), \end{aligned} \tag{7}$$

where

$$\tau_{l,m}^{(\mathrm{RT})} \triangleq \tau_l^{(\mathrm{F})} + \tau_m^{(\mathrm{B})} \tag{8}$$

represents the overall delay (i.e., the *round trip delay*) experienced by the signal radiated by lth TX antenna and captured by the considered RX antenna. The last signal travels from the RX antenna to the RF port of each of the two downconversion mixers (that are also fed by the waveforms generated by the VCO, as shown in Fig. 1); this introduces an additional (antenna dependent) delay, denoted $\tau_m^{(\mathrm{R})}$. Therefore, on the one hand, the signal applied to the RF port of the above mentioned mixers is given by

$$\begin{aligned} s_{l,m}^{(\mathrm{RF})}(t) &\triangleq s_{l,m}^{(\mathrm{RX})}(t - \tau_m^{(\mathrm{R})}) \\ &= s_I^{(\mathrm{VCO})}\left(t - \tau_l^{(\mathrm{TX})} - \tau_{l,m}^{(\mathrm{RT})} - \tau_m^{(\mathrm{R})}\right). \end{aligned} \tag{9}$$

On the other hand, the *local oscillator* (LO) ports of the same mixers are fed by the signals $s_I^{(\mathrm{VCO})}(t - \tau_m^{(\mathrm{LO})})$ (1) and $s_Q^{(\mathrm{VCO})}(t - \tau_m^{(\mathrm{LO})})$ (2); here, $\tau_m^{(\mathrm{LO})}$ denotes the delay experienced by both $s_I^{(\mathrm{VCO})}(t)$ and $s_Q^{(\mathrm{VCO})}(t)$ in travelling

[2]This assumption does not limit the generality of our analysis because the *superposition principle* can be easily applied in the case of multiple targets.

[3]In the following, the coordinates of the elements of the TX and RX arrays are also evaluated with respect to $\mathcal{O}$.

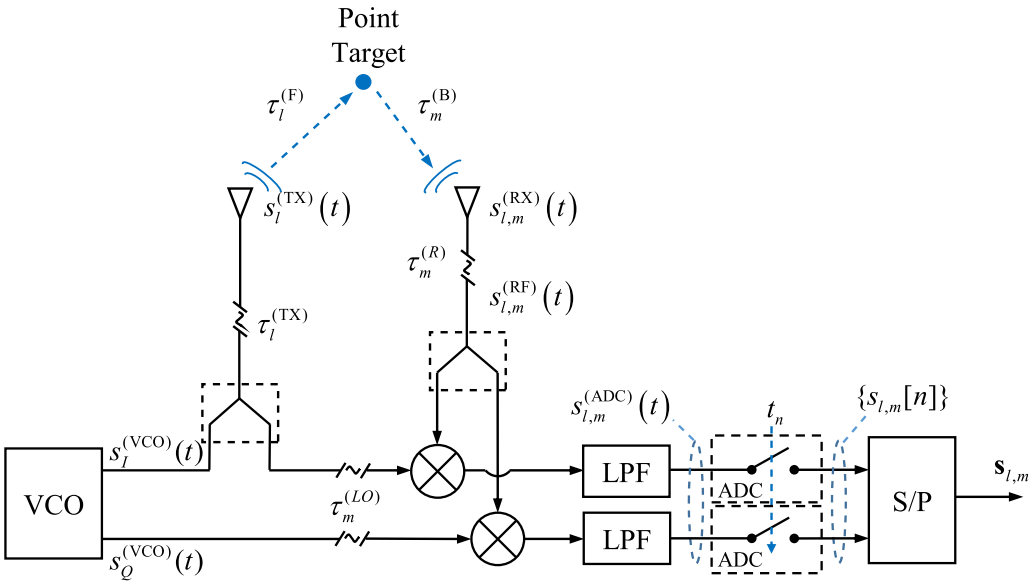

FIGURE 1. Representation of the signal chain involving the *l*th TX and *m*th RX antennas in the considered colocated MIMO radar. In this model, all the relevant delays originating from the employed hardware are highlighted.

along the two transmission lines that connect the VCO to the considered mixers. The signals available at the output of the two mixers undergo *low-pass filtering* (LPF; see Fig. 1); it is easy to show that the couple of the resulting *real* signals can be condensed in the single *complex* signal[4]

$$s_{l,m}^{(\mathrm{ADC})}(t) \simeq \exp\left(j\left(2\pi f_{l,m}^{(\mathrm{B})} t + \phi_{l,m}^{(\mathrm{B})}\right)\right), \tag{10}$$

where

$$f_{l,m}^{(\mathrm{B})} \triangleq 2\mu\left(\tau_l^{(\mathrm{TX})} + \tau_{l,m}^{(\mathrm{RT})} + \tau_m^{(\mathrm{RX})}\right) \tag{11}$$

and

$$\phi_{l,m}^{(\mathrm{B})} \triangleq 2\pi f_0\left(\tau_l^{(\mathrm{TX})} + \tau_{l,m}^{(\mathrm{RT})} + \tau_m^{(\mathrm{RX})}\right) \tag{12}$$

are the phase and frequency, respectively, of $s_{l,m}^{(\mathrm{ADC})}(t)$ and

$$\tau_m^{(\mathrm{RX})} \triangleq \tau_m^{(\mathrm{R})} - \tau_m^{(\mathrm{LO})} \tag{13}$$

represents the *total net delay* associated with each branch of the receiver. In the last part of the signal chain represented in Fig. 1, each of the two components of the signal $s_{l,m}^{(\mathrm{ADC})}(t)$ (10) is sampled at the instants $\{t_n = \tau_m^{(\mathrm{ADC})} + nT_s; n = 0, \ldots, N-1\}$ by an *analog-to-digital converter* (ADC); here, $\tau_m^{(\mathrm{ADC})}$ denotes an (antenna dependent) delay[5] due to analog-to-digital conversion, and $T_s = 1/f_s$ and

$$f_s \triangleq \frac{N}{T} \tag{14}$$

represent the ADC *sampling period* and its *sampling frequency*, respectively. Finally, the sequence of samples resulting from the analog-to-digital conversion undergoes serial-to-parallel conversion (accomplished by the S/P block in Fig. 1); this produces the N-dimensional row vector

$$\mathbf{s}_{l,m} \triangleq \left[s_{l,m}[0], s_{l,m}[1], \ldots, s_{l,m}[N-1]\right], \tag{15}$$

where $s_{l,m}[n] \triangleq s_{l,m}^{(\mathrm{ADC})}(t_n)$ for any n. This concludes our description of the signal chain represented in Fig. 1.

The mathematical results illustrated above deserve the following comments:

a) The overall delay appearing in the *right-hand side* (RHS) of both (11) and (12) can be seen as the sum of two terms: the first one is the round trip delay $\tau_{l,m}^{(\mathrm{RT})}$ (8), whereas the second one,

$$\begin{aligned}\tau_{l,m}^{(\mathrm{I})} &\triangleq \tau_l^{(\mathrm{TX})} + \tau_m^{(\mathrm{RX})} \\ &= \tau_l^{(\mathrm{TX})} + \tau_m^{(\mathrm{R})} - \tau_m^{(\mathrm{LO})},\end{aligned} \tag{16}$$

called *total net instrumental delay*, represents the contribution of the radar itself [25]. Note that the three terms contributing to $\tau_{l,m}^{(\mathrm{I})}$ do not have the same sign and that, in particular, $\tau_m^{(\mathrm{LO})}$ tends to partially cancel the contribution due to both $\tau_l^{(\mathrm{TX})}$ and $\tau_m^{(\mathrm{R})}$. Note also that $\tau_m^{(\mathrm{LO})}$ is often negligible in single chip radar devices, but can play an important role in cascaded devices.

b) Based on the considerations illustrated in the previous point, (11) and (12) can be rewritten as

$$f_{l,m}^{(\mathrm{B})} \triangleq f_{l,m}^{(\mathrm{RT})} + f_{l,m}^{(\mathrm{I})} \tag{17}$$

and

$$\phi_{l,m}^{(\mathrm{B})} \triangleq \phi_{l,m}^{(\mathrm{RT})} + \phi_{l,m}^{(\mathrm{I})} \tag{18}$$

[4]The following expression is approximate because it results from neglecting, in the phase of the complex exponential, all the quadratic terms that provide a negligible contribution to the phase itself. Despite this, it offers an accurate representation of the downconverted signal.

[5]The estimation of this parameter is out the scope of this manuscript; for this reason, it is not taken into consideration in the following.

respectively; here,

$$f_{l,m}^{(\mathrm{RT})} \triangleq 2\mu\tau_{l,m}^{(\mathrm{RT})} \tag{19}$$

and

$$\phi_{l,m}^{(\mathrm{RT})} \triangleq 2\pi f_0 \tau_{l,m}^{(\mathrm{RT})} \tag{20}$$

are the frequency and phase contributions, respectively, due to the round trip delay, whereas

$$f_{l,m}^{(\mathrm{I})} \triangleq 2\mu\tau_{l,m}^{(\mathrm{I})} = 2\mu\left(\tau_l^{(\mathrm{TX})} + \tau_m^{(\mathrm{RX})}\right) \tag{21}$$

and

$$\phi_{l,m}^{(\mathrm{I})} \triangleq 2\pi f_0 \tau_{l,m}^{(\mathrm{I})} = 2\pi f_0\left(\tau_l^{(\mathrm{TX})} + \tau_m^{(\mathrm{RX})}\right) \tag{22}$$

are the frequency and phase contributions, respectively, associated with the stray delays originating from the radar hardware [4]; the last two terms can be seen as a form of *frequency bias* and *phase bias*, respectively (or, equivalently, *frequency offset* and *phase offset*).

c) The contribution of $f_{l,m}^{(\mathrm{I})}$ to the beat frequency $f_{l,m}^{(\mathrm{B})}$ is much smaller than that of $f_{l,m}^{(\mathrm{RT})}$, since the delays $\tau_l^{(\mathrm{TX})}$ and $\tau_m^{(\mathrm{RX})}$ are significantly smaller than $\tau_{l,m}^{(\mathrm{RT})}$ (see (8) and (16)); on the other hand, the contribution of $\phi_{l,m}^{(\mathrm{I})}$ to the beat phase $\phi_{l,m}^{(\mathrm{B})}$ should not be ignored.

d) Eqs. (21) and (22) can be put in the form

$$f_{l,m}^{(\mathrm{I})} = f_l^{(\mathrm{TX})} + f_m^{(\mathrm{RX})} \tag{23}$$

and

$$\phi_{l,m}^{(\mathrm{I})} = \phi_l^{(\mathrm{TX})} + \phi_m^{(\mathrm{RX})}, \tag{24}$$

where

$$f_k^{(\mathrm{Z})} \triangleq 2\mu\tau_k^{(\mathrm{Z})} \tag{25}$$

and

$$\phi_k^{(\mathrm{Z})} \triangleq 2\pi f_0 \tau_k^{(\mathrm{Z})}, \tag{26}$$

represent the frequency and phase stray contributions, respectively, associated with the TX (RX) array kth antenna if Z = TX (Z = RX).

e) In FMCW radar systems, any frequency bias (see point b)) results in a *range bias*, since the range of any detected target is evaluated as [1]

$$R_{l,m} = \hat{f}_{l,m}^{(\mathrm{B})} \frac{c}{2\mu}, \tag{27}$$

where $\hat{f}_{l,m}^{(\mathrm{B})}$ denotes the frequency estimated at the RX side for the target itself. Consequently, the range bias affecting the kth TX (RX) antenna can be expressed as (see (25))

$$r_k^{(\mathrm{Z})} \triangleq c\tau_k^{(\mathrm{Z})} = f_k^{(\mathrm{Z})} \frac{c}{2\mu}, \tag{28}$$

with Z = TX (Z = RX), whereas that associated with the frequency bias $f_{l,m}^{(\mathrm{I})}$ (characterizing the lth TX and mth RX antennas) is given by

$$r_{l,m} = f_{l,m}^{(\mathrm{I})} \frac{c}{2\mu}. \tag{29}$$

f) The bias $f_{l,m}^{(\mathrm{I})}$ (21) is *antenna dependent* and, usually, is not large enough to represent a problem by itself, but may affect the accuracy of AoA estimation in radar imaging [4], [12], since the same target is detected at different ranges by distinct antennas. Similar considerations can be made for the phase bias $\phi_{l,m}^{(\mathrm{I})}$ (22). However, calibration is not required to fully compensate for the last bias, but to make it *antenna independent*; in fact, if this condition is met, the residual phase bias has no impact on imaging algorithms.

The phase and frequency calibration of the considered MIMO radar requires estimating the set $\{f_l^{(\mathrm{TX})}, f_m^{(\mathrm{RX})}, \phi_l^{(\mathrm{TX})}, \phi_m^{(\mathrm{RX})};\ l = 1, 2, \ldots, N_T,\ m = 1, 2, \ldots, N_R\}$, collecting $4N_TN_R$ distinct parameters, and compensating for their effects. This problem is tackled in two different ways in Sections III and IV.

III. TRADITIONAL CALIBRATION

In this section, the method for radar calibration presented in [4] and [28] is illustrated. When this method is adopted, a *reference target* must be positioned precisely in front of the MIMO radar to be calibrated and in its *far-field* region. This choice has the following implications:

1) The distance

$$R \triangleq \| \mathbf{o} \|_2 \tag{30}$$

of the reference target from the first TX antenna of the radar system satisfies the inequality

$$R \gg \frac{2D^2}{\lambda}, \tag{31}$$

where D is the largest Euclidean distance between TX and RX antennas of the radar array, and λ is the radar wavelength.

2) The parameter R represents, with good approximation, the distance of the reference target from each antenna of the radar array. Then, the approximations

$$\tau_l^{(\mathrm{F})} \simeq \tau_m^{(\mathrm{B})} \simeq \frac{R}{c} \tag{32}$$

and

$$\tau_{l,m}^{(\mathrm{RT})} \simeq 2\frac{R}{c}. \tag{33}$$

can be adopted for $\tau_l^{(\mathrm{F})}$ (4), $\tau_m^{(\mathrm{B})}$ (5) and $\tau_{l,m}^{(\mathrm{RT})}$ (8) for any l and m.

The TC method also requires the knowledge of reasonably accurate estimate[6] $\hat{R}$ of the target range R. This allows to compute the estimates

$$\hat{f}_{l,m}^{(\mathrm{RT})} \triangleq 4\mu\frac{\hat{R}}{c} \tag{34}$$

[6]In practice, a range error of a few centimeters is not of concern. However, if this error is antenna dependent, its presence results in range-angle coupling in AoA estimation. This negatively affects the quality of target estimates if the difference among the errors on all the antennas is greater than the range resolution of the considered radar system. This explains the importance of frequency compensation, which should make the range error *equal* on all the antennas. If the range of the reference target is known with high accuracy, then the range error is close to zero.

and

$$\hat{\phi}_{l,m}^{(\mathrm{RT})} \triangleq 4\pi f_0 \frac{\hat{R}}{c} \tag{35}$$

of the frequency $f_{l,m}^{(\mathrm{RT})}$ (19) and the phase $\phi_{l,m}^{(\mathrm{RT})}$ (20), respectively (note that both estimates are independent of the selected TX and RX antennas).

The first step of TC consists in computing an order N_0 *fast Fourier transform* (FFT) of the vector $\mathbf{s}_{l,m}$ (15) for any l and m; this produces the N_0-dimensional vector[7]

$$\mathbf{S}_{l,m} = \left[S_{l,m}[0], S_{l,m}[1], \ldots, S_{l,m}[N_0-1]\right] \triangleq \mathrm{FFT}_{N_0}\left[\mathbf{s}_{l,m}\right], \tag{36}$$

where $\mathrm{FFT}_{N_0}[\mathbf{x}]$ denotes the order N_0 FFT of the vector $\mathbf{x}$,

$$N_0 \triangleq N \cdot L, \tag{37}$$

and L represents the adopted *oversampling factor*. In TC it is assumed that the strongest electromagnetic echo detected by the considered radar system on each of its RX antennas (and independently of the employed TX antenna) is generated by the reference target. For this reason, the detection of that target and the estimation of its range can be accomplished through the *periodogram method*, i.e. by identifying the element of $\mathbf{S}_{l,m}$ having the highest amplitude; the index of this element can be expressed as

$$\hat{k}_{l,m}^{(\mathrm{B})} = \arg \max_{k \in \mathcal{S}_{N_0}} \left|S_{l,m}[k]\right|, \tag{38}$$

for any l and m; here,

$$\mathcal{S}_X \triangleq \{0, 1, \ldots, X-1\} \tag{39}$$

is a set collecting X consecutive integers. Given $\hat{k}_{l,m}^{(\mathrm{B})}$ (38), the estimates

$$\hat{f}_{l,m}^{(\mathrm{B})} = \hat{k}_{l,m}^{(\mathrm{B})} \frac{f_s}{N_0} \tag{40}$$

and

$$\hat{\phi}_{l,m}^{(\mathrm{B})} = \angle\ S_{l,m}\left[\hat{k}_{l,m}^{(\mathrm{B})}\right] \tag{41}$$

of the frequency $f_{l,m}^{(\mathrm{B})}$ (11) and the phase $\phi_{l,m}^{(\mathrm{B})}$ (12), respectively, characterizing the main tone detected in the sequence $\{s_{l,m}[n]\}$, are evaluated[8] for any l and m.

Then, substituting the *right hand side* (RHS) of (34) and (40) in that of (17) leads to the estimate

$$\hat{f}_{l,m}^{(\mathrm{I})} = \hat{k}_{l,m}^{(\mathrm{B})} \frac{f_s}{N_0} - 4\mu \frac{\hat{R}}{c} \tag{42}$$

of $f_{l,m}^{(\mathrm{I})}$ (23). Similarly, substituting the RHS of (35) and (41) in that of (18) produces the estimate

$$\hat{\phi}_{l,m}^{(\mathrm{I})} = \angle\ S_{l,m}\left[\hat{k}_{l,m}^{(\mathrm{B})}\right] - 4\pi f_0 \frac{\hat{R}}{c} \tag{43}$$

of $\phi_{l,m}^{(\mathrm{I})}$ (24). Given the sets $\{\hat{f}_{l,m}^{(\mathrm{I})}\}$ and $\{\hat{\phi}_{l,m}^{(\mathrm{I})}\}$ (each consisting of $N_T N_R$ elements), the estimates

$$\hat{f}_l^{(\mathrm{TX})} \triangleq \frac{1}{N_R}\sum_{m=1}^{N_R} \hat{f}_{l,m}^{(\mathrm{I})} - \frac{1}{N_T N_R}\sum_{l'=1}^{N_T}\sum_{m=1}^{N_R} \hat{f}_{l',m}^{(\mathrm{I})} \tag{44}$$

and

$$\hat{\phi}_l^{(\mathrm{TX})} \triangleq \frac{1}{N_R}\sum_{m=1}^{N_R} \hat{\phi}_{l,m}^{(\mathrm{I})} - \frac{1}{N_T N_R}\sum_{l'=1}^{N_T}\sum_{m=1}^{N_R} \hat{\phi}_{l',m}^{(\mathrm{I})} \tag{45}$$

of $f_l^{(\mathrm{TX})}$ and $\phi_l^{(\mathrm{TX})}$ (see (25) and (26), with Z = TX), respectively, are computed for the lth TX antenna (for any l). Similarly, the estimates

$$\hat{f}_m^{(\mathrm{RX})} \triangleq \frac{1}{N_T}\sum_{l=1}^{N_T} \hat{f}_{l,m}^{(\mathrm{I})} \tag{46}$$

and

$$\hat{\phi}_m^{(\mathrm{RX})} \triangleq \frac{1}{N_T}\sum_{l=1}^{N_T} \hat{\phi}_{l,m}^{(\mathrm{I})} \tag{47}$$

of $f_m^{(\mathrm{RX})}$ and $\phi_m^{(\mathrm{RX})}$ (see (25) and (26), with Z = RX), respectively, are evaluated for the mth RX antenna (for any m).

This concludes our description of the estimation procedure accomplished in TC.

Finally, it is worth pointing out that:

1) The frequency biases $\hat{f}_l^{(\mathrm{TX})}$ (44) and $\hat{f}_m^{(\mathrm{RX})}$ (46) can be easily converted into the corresponding range biases $\hat{r}_l^{(\mathrm{TX})}$ and $\hat{r}_m^{(\mathrm{RX})}$, respectively; this conversion can be accomplished through (28), with Z = TX and RX.

2) The TC method requires the reference target to be positioned perfectly in front of the radar system (and in its far-field region; see (31)) and its range R to be known with good accuracy. Moreover, any other target detectable in the considered propagation environment should not be close to the reference one and, in particular, should have a different range (otherwise its presence would represent a source of interference).

3) If the range R of the reference target is *unknown* (but that target is still in the far-field region of the radar system), (34) and (35) cannot be exploited. In this case, it can be assumed that

$$\hat{f}_{l,m}^{(\mathrm{RT})} = \min_{l,m}\left\{\hat{f}_{l,m}^{(\mathrm{B})}\right\} \tag{48}$$

and

$$\hat{\phi}_{l,m}^{(\mathrm{RT})} = 0 \tag{49}$$

for any l and m, where $\hat{f}_{l,m}^{(\mathrm{B})}$ and $\hat{\phi}_{l,m}^{(\mathrm{RT})}$ are expressed by (40) and (35) respectively. These choices result in frequency and phase offsets in the calibrated data; however, such offsets are independent of the selected pair of TX and RX antennas.

[7]The use of the FFT leads to discretizing the frequency domain (i.e., the range domain in a FMCW radar system) and, in particular, to partitioning it into N_0 frequency (i.e., range) *bins*.

[8]Note that a more accurate algorithm for the estimation of both parameters can be adopted in place of that proposed here (e.g., see [29] and references therein).

IV. MOVEMENT-BASED CALIBRATION

In this section, our movement-based approach to radar calibration is illustrated and two specific methods, called *far-field*-MBC (FF-MBC) and *near-field* MBC (NF-MBC), are proposed; the former method is used when the measurements acquired for radar calibration originate from targets positioned in the far-field region of the considered radar system, whereas the latter one relies on a reference target positioned in its near-field region. The description of both methods requires defining two distinct Cartesian coordinate systems to describe the radar movements; the first one, called *global system* and denoted $\mathcal{O}'$, is solidal to the propagation environment, whereas the other one, called *sensor system* and denoted $\mathcal{O}$, is solidal to the radar and has the same orientation as $\mathcal{O}'$. Therefore, we have that

$$\mathcal{O} = \mathcal{O}' + \mathbf{q}', \tag{50}$$

where $\mathbf{q}' = (q'_x, q'_y, q'_z)$ is a vector describing the translation that relates the two reference systems.

As shown in the following two subsections, both the FF-MBC and the NF-MBC involve the processing of multiple (say, N_m) measurements, each of which is acquired at a different position of the considered radar device in a completely static propagation environment. In practice, the radar device is moved along an horizontal rail and each new measurement is acquired after shifting the radar itself along the rail by a known quantity. For this reason, distinct measurements are characterized by different values of the vector $\mathbf{q}'$ in (50). The value of $\mathbf{q}'$ to be selected when the measurement originates from the lth TX and mth RX antennas is evaluated as follows. First of all, let us define:

a) The vector

$$\mathbf{v}_{l,m} \triangleq \frac{\mathbf{p}_l^{(\mathrm{TX})} + \mathbf{p}_m^{(\mathrm{RX})}}{2}, \tag{51}$$

that collects the barycentric coordinates (with respect to the sensor system $\mathcal{O}$) of the lth TX and mth RX antennas; here, $\mathbf{p}_l^{(\mathrm{TX})}$ and $\mathbf{p}_m^{(\mathrm{RX})}$ are defined by (6) with Z = TX and RX, respectively.

b) A *reference point*, having a fixed position with respect to $\mathcal{O}'$ and whose coordinates with respect to that reference system are collected in the vector $\mathbf{v}'$.

Then, the translation vector associated with the lth TX and mth RX antennas is computed as

$$\mathbf{q}'_{l,m} = \mathbf{v}' - \mathbf{v}_{l,m}. \tag{52}$$

In other words, each measurement is acquired after bringing the barycentric position of the considered couple of TX and RX antennas always to the same position (specified by $\mathbf{v}'$); this result is obtained by physically moving the radar without changing its orientation with respect to $\mathcal{O}'$.

Finally, it is important to point out that, in principle, the choice of the reference point is arbitrary; however, in practice, this point should be selected in a way that the barycenters of all the couples of TX and RX antennas can easily reach it (i.e., all the translations $\{\mathbf{q}'_{l,m}\}$ are really feasible by shifting the radar on the employed rail).

A. FAR-FIELD MOVEMENT-BASED CALIBRATION

If all the targets involved in radar calibration are in far-field, the following assumptions are made in MBC:

1) Each couple of TX-RX antennas of the considered MIMO radar can be represented as the antenna of a virtual *monostatic* radar, i.e., briefly, as a VA [30]. In particular, if the lth TX and mth RX antennas are considered, the position of the VA associated with this couple of physical antennas (briefly, the VA (l, m)) coincides with $\mathbf{v}_{l,m}$ (51) for any l and m. Note that, if N_T TX and N_R RX antennas are available, the overall number of VAs is $N_{VA} = N_T N_R$.

2) The electromagnetic echoes received by our radar system originate from an arbitrary number of (pointwise or extended) targets, but all positioned in the far-field region of the radar system. At least one target is required for radar calibration, but no additional requirement is given. It should be kept in mind, however, that the greater is the power returned by the set of targets, the larger is the *signal-to-noise ratio* (SNR) characterizing the resulting calibration matrix.

3) The difference between the distances of each couple of VAs from every target can be deemed negligible.[9]

In the following description of our approach to radar calibration, we can assume the presence of N_p detectable pointwise targets for simplicity. If R_p denotes the distance of the pth target from the reference point $\mathbf{v}'$ (with $p = 1, 2, \ldots, N_p$), the propagation delay experienced by an electromagnetic wave reflected by that target and reaching any VA of the MIMO radar is (see (8))

$$\tau_p^{(\mathrm{RT})} = \frac{2R_p}{c}, \tag{53}$$

so that the frequency and the phase associated with it are (see (19) and (20), respectively)

$$f_p^{(\mathrm{RT})} \triangleq 4\mu\frac{R_p}{c} \tag{54}$$

and

$$\phi_p^{(\mathrm{RT})} \triangleq 4\pi f_0 \frac{R_p}{c}, \tag{55}$$

respectively.

As already stated above, the proposed calibration method requires the availability of a set of N_m distinct measurements. As far as their acquisition is concerned, the following simple rules are adopted:

1) Each measurement originates from a different VA, so that $N_m = N_{VA}$.

2) All the measurements are always acquired after positioning the associated VAs exactly at the same point $\mathbf{v}'$ with respect to $\mathcal{O}'$. This requires shifting the considered radar device from measurement to measurement, without changing its spatial orientation.

[9] Note that this is a consequence of the far-field assumption.

In practice, the first measurement is acquired through a *reference* VA (say, the VA $(\bar{l}, \bar{m})$). Then, all the other measurements are obtained through the remaining $(N_{VA} - 1)$ VAs, after positioning each of the virtual elements at the same point as the VA $(\bar{l}, \bar{m})$.

The baseband signal made available by the VA (l, m) can be expressed as[10]

$$s_{l,m}^{(\mathrm{ADC})}(t) = \sum_{p=1}^{N_p} \exp\left(j\left(2\pi f_p^{(\mathrm{RT})} t + \phi_p^{(\mathrm{RT})}\right)\right) \times \exp\left(j\left(2\pi f_{l,m}^{(\mathrm{I})} t + \phi_{l,m}^{(\mathrm{I})}\right)\right) \tag{56}$$

for $t \in [0, T)$, and for any l and m. Similarly as TC, the last signal undergoes analog-to-digital conversion; this produces the N-dimensional vector $\mathbf{s}_{l,m}$ (see (15)), that, after zero padding, undergoes an order N_0 FFT, whose output is the N_0-dimensional vector $\mathbf{S}_{l,m}$ (see (36) and (37)). However, the remaining processing steps are substantially different from those accomplished in TC. In fact, first of all, since the VA $(\bar{l}, \bar{m})$ is taken as a reference antenna, it is assumed that

$$f_{\bar{l},\bar{m}}^{(\mathrm{I})} = 0, \tag{57}$$

i.e., that, for this VA, the frequency shift appearing in the RHS of (56) is equal to zero. Then, for any $(l, m) \neq (\bar{l}, \bar{m})$, the frequency shift $f_{l,m}^{(\mathrm{I})}$ associated with the VA (l, m) is estimated by: a) computing the correlation between the amplitude spectrum referring to the reference antenna and that referring to the VA (l, m); b) evaluating the positive or negative frequency shift associated with the correlation peak. In practice, we first extract the portion of the spectrum $\mathbf{S}_{l,m}$ associated with the far-field region; that portion is conveyed by the d-dimensional vector

$$\begin{aligned}\mathbf{U}_{l,m} &= \left[U_{l,m}[0], \ldots, U_{l,m}[d-1]\right] \\ &\triangleq \left[S_{l,m}[\bar{k}], \ldots, S_{l,m}[N_0 - 1]\right],\end{aligned} \tag{58}$$

where $d \triangleq N_0 - \bar{k}$,

$$\bar{k} \triangleq \left\lceil 2N_0 \frac{cD^2}{\mu \lambda f_s} \right\rceil \tag{59}$$

represents the index of the first bin associated with the far-field region (see (31)) and $\lceil \cdot \rceil$ represents the *ceiling function*. Then, the estimate $\hat{f}_{l,m}^{(\mathrm{I})}$ of the frequency mismatch $f_{l,m}^{(\mathrm{I})}$ with respect to the reference antenna is evaluated as[11]

$$\hat{f}_{l,m}^{(\mathrm{I})} = \frac{f_s}{N_0}\left(\arg\max_{n \in \mathcal{S}_d}\left\{c_{l,m}[n]\right\} - \frac{d}{2}\right) \tag{60}$$

for any l and m; here,

$$c_{l,m}[n] = \sum_{k=0}^{d-1} \left|W_{\bar{l},\bar{m}}[k+n]\right| \left|U_{l,m}[k]\right| \tag{61}$$

is the correlation between the amplitude spectrum of the VA (l, m) and $(2d-1)$-dimensional vector

$$\begin{aligned}\mathbf{W}_{\bar{l},\bar{m}} &= \left[W_{\bar{l},\bar{m}}[0], W_{\bar{l},\bar{m}}[1], \ldots, W_{\bar{l},\bar{m}}[2d-1]\right] \\ &\triangleq \left[\mathbf{W}_{\bar{l},\bar{m}}^{(\mathrm{L})}, \mathbf{W}_{\bar{l},\bar{m}}^{(\mathrm{C})}, \mathbf{W}_{\bar{l},\bar{m}}^{(\mathrm{U})}\right]\end{aligned} \tag{62}$$

that represents a *cyclically extended version* of the amplitude spectrum of the reference VA, since

$$\mathbf{W}_{\bar{l},\bar{m}}^{(\mathrm{L})} \triangleq \left[U_{\bar{l},\bar{m}}[d/2], U_{\bar{l},\bar{m}}[d/2+1], \ldots, U_{\bar{l},\bar{m}}[d-1]\right], \tag{63}$$

$$\mathbf{W}_{\bar{l},\bar{m}}^{(\mathrm{C})} \triangleq \left[U_{\bar{l},\bar{m}}[0], U_{\bar{l},\bar{m}}[1], \ldots, U_{\bar{l},\bar{m}}[d-1]\right] \tag{64}$$

and

$$\mathbf{W}_{\bar{l},\bar{m}}^{(\mathrm{U})} \triangleq \left[U_{\bar{l},\bar{m}}[0], U_{\bar{l},\bar{m}}[1], \ldots, U_{\bar{l},\bar{m}}[d/2-1]\right]. \tag{65}$$

Once the estimate $\hat{f}_{l,m}^{(\mathrm{I})}$ (60) has been computed for any $(l, m) \neq (\bar{l}, \bar{m})$, the spectrum of the VA (l, m) can be aligned with that of the reference antenna by applying a frequency shift to the elements of the time domain vector $\mathbf{s}_{l,m}$ associated with $\mathbf{S}_{l,m}$, i.e. by computing [4]

$$s_{l,m}^{(\mathrm{FC})}[k] = s_{l,m}[k] \exp\left(-j2\pi \hat{f}_{l,m}^{(\mathrm{I})} k T_s\right) \tag{66}$$

for $k = 0, 1, \ldots, N-1$. These samples are collected in the vector

$$\mathbf{s}_{l,m}^{(\mathrm{FC})} = \left[s_{l,m}^{(\mathrm{FC})}[0], s_{l,m}^{(\mathrm{FC})}[1], \ldots, s_{l,m}^{(\mathrm{FC})}[N-1]\right], \tag{67}$$

that feeds an order N FFT; this produces the N-dimensional vector

$$\begin{aligned}\mathbf{S}_{l,m}^{(\mathrm{FC})} &\triangleq \mathrm{FFT}_N\left[\mathbf{s}_{l,m}^{(\mathrm{FC})}\right] \\ &= \left[S_{l,m}^{(\mathrm{FC})}[0], S_{l,m}^{(\mathrm{FC})}[1], \ldots, S_{l,m}^{(\mathrm{FC})}[N-1]\right].\end{aligned} \tag{68}$$

Given this vector, the estimate[12]

$$\hat{\phi}_{l,m}^{(\mathrm{I})} \triangleq \angle\left\{\sum_{k=\hat{k}}^{N}\left(\frac{S_{l,m}^{(\mathrm{FC})}[k]}{S_{\bar{l},\bar{m}}^{(\mathrm{FC})}[k]}\left|S_{\bar{l},\bar{m}}^{(\mathrm{FC})}[k]\right|^2\right)\right\} \tag{69}$$

of the instrumental phase $\phi_{l,m}^{(\mathrm{I})}$ is evaluated for any l and m; here, $\hat{k}$ is an integer parameter whose definition is obtained from that of $\bar{k}$ (59) by simply replacing N_0 with N. Given the sets $\{\hat{f}_{l,m}^{(\mathrm{I})}\}$ and $\{\hat{\phi}_{l,m}^{(\mathrm{I})}\}$, the estimates of the phase shifts $\{\hat{\phi}_l^{(\mathrm{TX})}, \hat{\phi}_m^{(\mathrm{RX})}\}$ and those of the frequency shifts $\{\hat{f}_l^{(\mathrm{TX})}, \hat{f}_m^{(\mathrm{RX})}\}$ characterizing all the elements of both the TX and RX arrays are evaluated according to (44)-(47). This concludes our description of the parameter estimation procedure accomplished in FF-MBC; this procedure is summarized in Algorithm 1.

Finally, it is worth pointing out that:

1) The squared term $|S_{\bar{l},\bar{m}}^{(\mathrm{FC})}[k]|^2$ appearing in the RHS of (69) does not modify the phase of the ratio $S_{l,m}^{(\mathrm{FC})}[k]/S_{\bar{l},\bar{m}}^{(\mathrm{FC})}[k]$

[10] Note that: a) the following model generalizes that expressed by (10), that refers to the case $N_p = 1$; b) the second factor appearing in the phase of its complex exponential does not depend on the target index p (i.e., it represents a phase & frequency shift influencing the echoes produced by different targets in the same way).

[11] From the following equation it is easily inferred that $\hat{f}_{\bar{l},\bar{m}}^{(\mathrm{I})} = 0$.

[12] From the following equation it is easily inferred that $\hat{\phi}_{\bar{l},\bar{m}}^{(\mathrm{I})} = 0$.

Algorithm 1 Far-field MBC

1: Place the radar to be calibrated in a static propagation environment characterized by multiple (pointwise or extended) targets in far-field. Select the reference VA (corresponding to $(l, m) = (\bar{l}, \bar{m})$).
2: **for** $l = 1$ to $l = N_T$ **do**
3: **for** $m = 1$ to $m = N_R$ **do**
4: Move the radar according to the translation vector $\mathbf{q}'_{l,m}$ (see (52)).
5: Acquire the N-dimensional vector $\mathbf{s}_{l,m}^{(\mathrm{ADC})}$ from the VA (l, m).
6: Compute the N_0-dimensional vector $\mathbf{S}_{l,m}$ on the basis of (36).
7: **end for**
8: **end for**
9: Extract the vector $\mathbf{U}_{l,m}$ from $\mathbf{S}_{l,m}$ (see (58) and (59)) for any l and m.
10: Generate the cyclically extended version $\mathbf{W}_{\bar{l},\bar{m}}$ of $\mathbf{U}_{\bar{l},\bar{m}}$ according to (62).
11: Compute the correlation sequence $\{c_{l,m}[n]\}$ and the frequency estimate $\hat{f}_{l,m}^{(\mathrm{I})}$ on the basis of (61) and (60), respectively, for any $(l, m) \neq (\bar{l}, \bar{m})$.
12: Compute the vectors $\mathbf{s}_{l,m}^{(\mathrm{FC})}$ and $\mathbf{S}_{l,m}^{\mathrm{FC}}$, and the phase estimate $\hat{\phi}_{l,m}^{(\mathrm{I})}$ on the basis of (67), (68) and (69), respectively, for any $(l, m) \neq (\bar{l}, \bar{m})$.
13: Compute the phase estimates $\{\hat{\phi}_l^{(\mathrm{TX})}, \hat{\phi}_m^{(\mathrm{RX})}\}$ and the frequency estimates $\{\hat{f}_l^{(\mathrm{TX})}, \hat{f}_m^{(\mathrm{RX})}\}$ according to (44)-(47) for any l and m.

and aims at emphasizing the contribution of strongest reflections (i.e., at increasing the SNR in phase estimation).

2) The estimate $\hat{\phi}_{l,m}^{(\mathrm{I})}$ of the instrumental phase $\phi_{l,m}^{(\mathrm{I})}$ evaluated on the basis of (69) does not require any knowledge about the overall number of targets (i.e., N_p) and their positions.

3) The selection of the reference antenna $VA(\bar{l}, \bar{m})$ is arbitrary; as already pointed out above, both the frequency shift $\hat{f}_{\bar{l},\bar{m}}^{(\mathrm{I})}$ and the phase shift $\hat{\phi}_{\bar{l},\bar{m}}^{(\mathrm{I})}$ associated with it are equal to zero.

B. NEAR-FIELD MOVEMENT-BASED CALIBRATION

The calibration procedure described in the previous subsection cannot be applied to the near-field scenario as it is since, in this case, the two way delay of each echo must be evaluated separately for each couple of TX and RX antennas. Moreover, in contrast to far-field scenario, where there is no reference target, a pointwise reference target is needed. This target is put in a point close to the radar and whose coordinate vector (with respect to the global system $\mathcal{O}'$) is denoted $\mathbf{o}' = (x_{o'}, y_{o'}, z_{o'})$. Its position is approximately known;[13] however, it is required that its range is not equal or similar to that of any other target detectable in the considered propagation environment.

Given these assumptions, the derivation of the NF-MBC procedure can be summarized as follows. The time intervals the signal radiated by the the l th TX antenna takes to reach the reference target and to travel from this to the mth RX antenna can be expressed as (see (4) and (5), respectively)

$$\tau_{l,m}^{(\mathrm{F})}(\mathbf{o}') = \frac{1}{c}\left\|\mathbf{o}' - \mathbf{p}'^{(\mathrm{TX})}_{l,m}\right\|_2 \tag{70}$$

and

$$\tau_{l,m}^{(\mathrm{B})}(\mathbf{o}') = \frac{1}{c}\left\|\mathbf{o}' - \mathbf{p}'^{(\mathrm{RX})}_{l,m}\right\|_2, \tag{71}$$

respectively, where

$$\mathbf{p}'^{(\mathrm{RX})}_{l,m} = \mathbf{p}_m^{(\mathrm{RX})} - \mathbf{q}'_{l,m} \tag{72}$$

and

$$\mathbf{p}'^{(\mathrm{TX})}_{l,m} = \mathbf{p}_l^{(\mathrm{TX})} - \mathbf{q}'_{l,m} \tag{73}$$

are the positions (with respect to the global system $\mathcal{O}'$) of the lth TX and mth RX antennas, respectively, $\mathbf{q}'_{l,m}$ is the translation vector relating our two reference systems (see (52)), $\mathbf{v}'$ is the coordinate vector (evaluated with respect to $\mathcal{O}'$) of a fixed *reference point* and $\mathbf{v}_{l,m}$ is expressed by (51) (i.e., it identifies the position of the barycenter[14] of the lth TX and mth RX antennas). Therefore, the overall propagation delay characterizing the lth TX and the mth RX antennas is (see (8))

$$\tau_{l,m}^{(\mathrm{RT})}(\mathbf{o}') = \tau_{l,m}^{(\mathrm{F})}(\mathbf{o}') + \tau_{l,m}^{(\mathrm{B})}(\mathbf{o}'). \tag{74}$$

Substituting the RHS of the last formula in (19) and (20) and, then, the resulting formulas in (10) allows us to express the couple of real input signals of the ADCs connected to the mth RX antenna in complex form as

$$\begin{aligned} s_{l,m}^{(\mathrm{ADC})}(t; \mathbf{o}') = &\exp\left(j\left(2\pi f_{l,m}^{(\mathrm{RT})}(\mathbf{o}')t + \phi_{l,m}^{(\mathrm{RT})}(\mathbf{o}')\right)\right) \\ &\times \exp\left(j\left(2\pi f_{l,m}^{(\mathrm{I})}t + \phi_{l,m}^{(\mathrm{I})}\right)\right) \end{aligned} \tag{75}$$

for t $\in [0, T)$, and for any l and m. Sampling this signal at the N instants $\{t_k = kT_s; k = 0, 1, \ldots, N-1)\}$ generates the elements of the N-dimensional vector[15] $\mathbf{s}_{l,m}$ (see 15), with $s_{l,m}[k] \triangleq s_{l,m}^{(\mathrm{ADC})}(t_k; \mathbf{o}')$ for $k = 0, 1, \ldots, N-1$. Similarly as FF-MBC, this vector feeds an order N_0 FFT, producing the N_0-dimensional vector $\mathbf{S}_{l,m}$ (see (36); the parameter N_0 is still defined by (37)). Based on this vector, the estimates $\hat{f}_{l,m}^{(\mathrm{B})}$ and $\hat{\phi}_{l,m}^{(\mathrm{B})}$ of $f_{l,m}^{(\mathrm{B})}$ (11) and $\phi_{l,m}^{(\mathrm{B})}$ (12), respectively, are evaluated according to[16] (40) and (41), respectively, where $\hat{k}_{l,m}$ is still

[13] It can be accurately estimated, as shown in the following.

[14] As a matter of fact, the position of this barycenter coincides with that of the VA (l, m); however, the VA concept is not mentioned in this subsection, in order to avoid any confusion.

[15] In the following, the dependence of this and other vectors on $\mathbf{o}'$ is omitted to simplify the notation.

[16] Similarly as TC, more refined algorithms different from the periodogram method can be used to to estimate $\hat{f}_{l,m}^{(\mathrm{B})}$ and $\hat{\phi}_{l,m}^{(\mathrm{B})}$ in this case.

expressed by (38). Then, based on (17) and (18), we can state that, if $f_{l,m}^{(\mathrm{RT})}(\mathbf{o}')$ and $\phi_{l,m}^{(\mathrm{RT})}(\mathbf{o}')$ were known, the estimate

$$\hat{f}_{l,m}^{(\mathrm{I})} = \hat{f}_{l,m}^{(\mathrm{B})} - f_{l,m}^{(\mathrm{RT})}(\mathbf{o}') \tag{76}$$

of the frequency $f_{l,m}^{(\mathrm{I})}$ (21) and the estimate

$$\hat{\phi}_{l,m}^{(\mathrm{I})} = \hat{\phi}_{l,m}^{(\mathrm{B})} - \phi_{l,m}^{(\mathrm{RT})}(\mathbf{o}') \tag{77}$$

of the phase $\phi_{l,m}^{(\mathrm{I})}$ (22) could be easily evaluated. However, since $\mathbf{o}'$ is not perfectly known, the values of the frequency $f_{l,m}^{(\mathrm{RT})}(\mathbf{o}')$ and the phase $\phi_{l,m}^{(\mathrm{RT})}(\mathbf{o}')$ are unavailable and, consequently, have to be estimated as well. A simple method for estimating this couple of parameters can be devised as follows. To begin, let us replace $f_{l,m}^{(\mathrm{RT})}(\mathbf{o}')$ with $\tilde{f}_{l,m}^{(\mathrm{RT})}(\tilde{\mathbf{o}}')$ in (76) and, similarly, $\phi_{l,m}^{(\mathrm{RT})}(\mathbf{o}')$ with $\tilde{\phi}_{l,m}^{(\mathrm{RT})}(\tilde{\mathbf{o}}')$ in (77); here, $\tilde{\mathbf{o}}'$ represents a trial value of $\mathbf{o}'$, and $\tilde{f}_{l,m}^{(\mathrm{RT})}(\tilde{\mathbf{o}}')$ and $\tilde{\phi}_{l,m}^{(\mathrm{RT})}(\tilde{\mathbf{o}}')$ denote the trial values of $f_{l,m}^{(\mathrm{RT})}$ and $\phi_{l,m}^{(\mathrm{RT})}$, respectively, associated with $\mathbf{o}' = \tilde{\mathbf{o}}'$. This yields

$$\tilde{f}_{l,m}^{(\mathrm{I})}(\tilde{\mathbf{o}}') = \hat{f}_{l,m}^{(\mathrm{B})} - \tilde{f}_{l,m}^{(\mathrm{RT})}(\tilde{\mathbf{o}}') \tag{78}$$

and

$$\tilde{\phi}_{l,m}^{(\mathrm{I})}(\tilde{\mathbf{o}}') = \hat{\phi}_{l,m}^{(\mathrm{B})} - \tilde{\phi}_{l,m}^{(\mathrm{RT})}(\tilde{\mathbf{o}}'). \tag{79}$$

Then, we note that the phase $\tilde{\phi}_{l,m}^{(\mathrm{I})}(\tilde{\mathbf{o}}')$ can be represented as the sum of two terms, namely the true value $\phi_{l,m}^{(\mathrm{I})}$ (22) and an error term, denoted $\varepsilon_{l,m}^{(\Phi)}(\tilde{\mathbf{o}}')$ and depending on $\tilde{\mathbf{o}}'$ (this error is expected to become smaller as $\tilde{\mathbf{o}}'$ approaches $\mathbf{o}'$). This consideration allows us to express the phase $\tilde{\phi}_{l,m}^{(\mathrm{I})}(\tilde{\mathbf{o}}')$ as

$$\tilde{\phi}_{l,m}^{(\mathrm{I})}(\tilde{\mathbf{o}}') = 2\pi f_0 \left(\tau_l^{(\mathrm{TX})} + \tau_m^{(\mathrm{RX})}\right) + \varepsilon_{l,m}^{(\Phi)}(\tilde{\mathbf{o}}'). \tag{80}$$

Let us define now:

a) The $N_T \times N_R$ *instrumental phase matrix* $\tilde{\Phi}^{(\mathrm{I})}(\tilde{\mathbf{o}}') = \left[\tilde{\phi}_{l,m}^{(\mathrm{I})}(\tilde{\mathbf{o}}')\right]$ and the $(N_T - 1) \times N_R$ *differential phase matrix*[17]

$$\tilde{\Phi}^{(\mathrm{D})}(\tilde{\mathbf{o}}') = \left[\tilde{\phi}_{l,m}^{(\mathrm{D})}(\tilde{\mathbf{o}}')\right] \tag{81}$$

where

$$\tilde{\phi}_{l,m}^{(\mathrm{D})}(\tilde{\mathbf{o}}') \triangleq \tilde{\phi}_{l+1,m}^{(\mathrm{I})}(\tilde{\mathbf{o}}') - \tilde{\phi}_{l,m}^{(\mathrm{I})}(\tilde{\mathbf{o}}'), \tag{82}$$

for $l = 1, 2, \ldots, N_T - 1$ and $m = 1, 2, \ldots, N_R$.

b) The $(N_T - 1) \times (N_R - 1)$ *error matrix*[18]

$$\tilde{\Phi}^{(\mathrm{E})}(\tilde{\mathbf{o}}') = \left[\tilde{\phi}_{l,m}^{(\mathrm{E})}(\tilde{\mathbf{o}}')\right] \tag{83}$$

where

$$\tilde{\phi}_{l,m}^{(\mathrm{E})}(\tilde{\mathbf{o}}') \triangleq \tilde{\phi}_{l,m+1}^{(\mathrm{D})}(\tilde{\mathbf{o}}') - \tilde{\phi}_{l,m}^{(\mathrm{D})}(\tilde{\mathbf{o}}') \tag{84}$$

for $l = 1, 2, \ldots, N_T - 1$ and $m = 1, 2, \ldots, N_R - 1$.

[17]This matrix results from evaluating the element-by-element difference of adjacent columns of $\tilde{\Phi}^{(\mathrm{I})}(\tilde{\mathbf{o}}')$ (i.e., of columns referring to distinct RX antennas).

[18]This matrix results from evaluating the element-by-element difference of adjacent rows of $\tilde{\Phi}^{(\mathrm{D})}(\tilde{\mathbf{o}}')$ (i.e., of rows referring to distinct TX antennas).

The elements of the matrices $\tilde{\Phi}^{(\mathrm{D})}(\tilde{\mathbf{o}}')$ (81) and $\tilde{\Phi}^{(\mathrm{E})}(\tilde{\mathbf{o}}')$ (83) have some relevant properties. In fact, substituting the RHS of (80) in that of (82) yields

$$\tilde{\phi}_{l,m}^{(\mathrm{D})}(\tilde{\mathbf{o}}') = 2\pi f_0 \left(\tau_{l+1}^{(\mathrm{TX})} - \tau_l^{(\mathrm{TX})}\right) + \varepsilon_{l+1,m}^{(\Phi)}(\tilde{\mathbf{o}}') - \varepsilon_{l,m}^{(\Phi)}(\tilde{\mathbf{o}}'). \tag{85}$$

The last results entails that $\tilde{\phi}_{l,m}^{(\mathrm{D})}(\tilde{\mathbf{o}}')$ does not depend on the delay $\tau_m^{(\mathrm{RX})}$ for any l and m; this is due to the fact that the dependence on that delay is cancelled by the subtraction appearing in the RHS of (82). Similary, substituting the RHS of (85) in that of (84) yields

$$\tilde{\phi}_{l,m}^{(\mathrm{E})}(\tilde{\mathbf{o}}') = \varepsilon_{l+1,m+1}^{(\Phi)}(\tilde{\mathbf{o}}') - \varepsilon_{l,m+1}^{(\Phi)}(\tilde{\mathbf{o}}') - \varepsilon_{l+1,m}^{(\Phi)}(\tilde{\mathbf{o}}') + \varepsilon_{l,m}^{(\Phi)}(\tilde{\mathbf{o}}'). \tag{86}$$

From the last result it is easily inferred that:

a) The matrix $\tilde{\Phi}^{(\mathrm{E})}(\tilde{\mathbf{o}}')$ (83) is independent not only of the delays $\{\tau_m^{(\mathrm{RX})}\}$, but also of the delays $\{\tau_l^{(\mathrm{TX})}\}$; this property originates from the one illustrated above for the elements of the matrix $\tilde{\Phi}^{(\mathrm{D})}(\tilde{\mathbf{o}}')$ (81) and from the subtraction appearing in the RHS of (84).

b) An estimate of $\mathbf{o}'$ can be evaluated by minimizing the absolute value of the elements of the matrix $\tilde{\Phi}^{(\mathrm{E})}(\tilde{\mathbf{o}}')$, since they can be expressed as a superposition of the error terms $\{\varepsilon_{l,m}^{(\Phi)}(\tilde{\mathbf{o}}')\}$.

In our work, based on the last consideration, the estimate $\hat{\mathbf{o}}'$ of $\mathbf{o}'$ is evaluated as

$$\hat{\mathbf{o}}' = \arg\min_{\tilde{\mathbf{o}}'} \sum_{l=1}^{N_T-1} \sum_{m=1}^{N_R-1} \left|\tilde{\phi}_{l,m}^{(\mathrm{E})}(\tilde{\mathbf{o}}')\right|. \tag{87}$$

Note that the computation of $\tilde{\phi}_{l,m}^{(\mathrm{E})}(\tilde{\mathbf{o}}')$ for a given value of $\tilde{\mathbf{o}}'$ is based on (20), (70),(71), (74), (77), (82) and (84).

Unluckily, the optimization problem (87) may not admit a unique solution and need to be solved numerically. The method we have adopted to solve it in an approximate fashion can be summarized as follows. First of all, the trial position of the target is expressed in spherical coordinates, i.e. as

$$\tilde{\mathbf{o}}' = (\tilde{R}_{o'}, \tilde{\theta}_{o'}, \tilde{\psi}_{o'}), \tag{88}$$

where $\tilde{R}_{o'}$, $\tilde{\theta}_{o'}$ and $\tilde{\psi}_{o'}$ denote the trial values of target range, azimuth and elevation, respectively. Then, it is assumed that accurate estimates $\hat{\theta}_{o'}$ and $\hat{\psi}_{o'}$ of the target azimuth $\theta_{o'}$ and elevation $\psi_{o'}$, respectively, are available. Under this assumption, the optimization problem (87) can be easily reformulated as a *one-dimensional* (1D) optimization problem involving the variable $\tilde{R}_{o'}$, i.e. as

$$\hat{R}_{o'} = \arg\min_{\tilde{R}_{o'}} \sum_{l=1}^{N_T-1} \sum_{m=1}^{N_R-1} \left|\tilde{\phi}_{l,m}^{(\mathrm{E})}(\tilde{R}_{o'}, \hat{\theta}_{o'}, \hat{\psi}_{o'})\right|, \tag{89}$$

since $\hat{\mathbf{o}}' = (\hat{R}_{o'}, \hat{\theta}_{o'}, \hat{\psi}_{o'})$. Therefore, if an approximate knowledge of the target range is available, the last problem can be easily solved by performing an exhaustive search over a relatively small grid of trial values for $R_{o'}$.

As far as the evaluation of $\hat{\theta}_{o'}$ and $\hat{\psi}_{o'}$ is concerned, the following procedure is employed. A single couple of TX and RX antennas is selected to acquire N_m measurements at N_m different positions; this is tantamount to: a) using the MIMO radar as if it was a SISO device; b) exploiting the *synthetic aperture* built up through its movement. Then, the available measurements undergo *three-dimensional* (3D) FFT processing; finally, $\hat{\theta}_{o'}$ and $\hat{\psi}_{o'}$ are evaluated through a peak search in the resulting amplitude spectrum. In doing so, it should be kept in mind that, in 3D FFT processing, the range, azimuth and elevation orders, denoted $N_0^{(R)}$, $N_0^{(\theta)}$ and $N_0^{(\psi)}$, respectively, should be large enough to ensure an accurate estimation of the spatial coordinates of the reference target; further details about this are provided in Section V.

Once $\hat{\mathbf{o}}'$ is available, the estimates $\hat{f}_{l,m}^{(\mathrm{I})}$ and $\hat{\phi}_{l,m}^{(\mathrm{I})}$ of $f_{l,m}^{(\mathrm{I})}$ (21) and $\phi_{l,m}^{(\mathrm{I})}$ (22) are evaluated through the following three steps: a) setting $\mathbf{o}' = \hat{\mathbf{o}}'$ in (70) and (71); b) substituting the resulting value of $\tau_{l,m}^{(\mathrm{RT})}$ in (19) and (20); c) computing (76) and (77). Then, the estimates $\{\hat{\phi}_l^{(\mathrm{TX})}, \hat{\phi}_m^{(\mathrm{RX})}\}$ and $\{\hat{f}_l^{(\mathrm{TX})}, \hat{f}_m^{(\mathrm{RX})}\}$ of the TX & RX phase shifts and frequency shifts, respectively, are computed according to (44)-(47).

To conclude, it is worth stress that, unlike FF-MBC and TC, NF-MBC is able of estimate the *absolute* range bias for each couple of TX and RX antennas without the need of selecting a reference couple (i.e. without the need to rely on assumptions like those expressed by (48) or (57)), provided that a reliable estimate of the angular coordinates of the reference target can be obtained.

C. IMPLEMENTATION OF MOVEMENT-BASED CALIBRATION

Let us assume, for simplicity, that the considered MIMO radar device is equipped with a 1D array and, in particular, with a *virtual uniform linear array* (VULA) consisting of N_{VA} VAs (see Fig. 2-a). In this case, we have that:

1) The FF-MBC method can be implemented by moving the considered device along an horizontal rail, as exemplified by Fig. 2-a), that refers to the case in which the overall length of the array is equal to L_{VA}. The objective of the radar movement is to sequentially put each VA of the array in the same specific point, namely in the *reference point*, that has a fixed position with respect to the reference system $\mathcal{O}'$ (such a position is identified by the vector $\mathbf{v}'$). Therefore, the radar on the rail always observes any target from a single fixed point, even if through different antennas.

2) At the end of the acquisition procedure, N_{VA} distinct measurements become available, one for each of the N_{VA} positions of the radar device. In fact, the VA providing a given measurement is the one positioned at the reference point. In practice, in the considered case, the first measurement originates from the rightmost VA of the array (see Fig. 2-b) and the last one from the leftmost VA (see Fig. 2-c).

3) After acquiring a new measurement, the device is moved from left to right by the interantenna spacing d_a, which is usually equal to $\lambda/4$.

Algorithm 2 Near-field MBC

1: Place a reference target in front of the radar to be calibrated (a precise alignment is not required) and estimate its range in an approximate fashion.
2: **for** $l = 1$ to $l = N_T$ **do**
3: **for** $m = 1$ to $m = N_R$ **do**
4: Move the radar according to the translation vector $\mathbf{q}'_{l,m}$ (see (52)).
5: Acquire the N-dimensional vector $\mathbf{s}_{l,m}^{(\mathrm{ADC})}$ from the mth RX antenna when the lth TX antenna is active.
6: Compute the estimates $\hat{f}_{l,m}^{(\mathrm{B})}$ and $\hat{\phi}_{l,m}^{(\mathrm{B})}$ on the basis of (40) and (41), respectively.
7: **end for**
8: **end for**
9: Compute the estimates $\hat{\theta}_{o'}$ and $\hat{\psi}_{o'}$ of the target azimuth $\theta_{o'}$ and elevation $\psi_{o'}$, respectively, of the reference target; this requires: a) exploiting the *synthetic aperture* built up through the movement of a single couple of TX and RX antennas; b) applying the periodogram method to the acquired measurements.
10: **for** multiple values of the trial target range $\tilde{R}_{\mathbf{o}'}$ **do**
11: Compute the corresponding trial values $\tilde{f}_{l,m}^{(\mathrm{RT})}$, $\tilde{\phi}_{l,m}^{(\mathrm{RT})}$, $\tilde{f}_{l,m}^{(\mathrm{I})}$ and $\tilde{\phi}_{l,m}^{(\mathrm{I})}$ of $f_{l,m}^{(\mathrm{RT})}$, $\phi_{l,m}^{(\mathrm{RT})}$, $f_{l,m}^{(\mathrm{I})}$ and $\phi_{l,m}^{(\mathrm{I})}$, respectively, on the basis of (17)-(20) for any l and m.
12: Compute the error matrix $\tilde{\Phi}^{(\mathrm{E})}(\tilde{\mathbf{o}}')$ (83) and store it.
13: **end for**
14: Evaluate the estimate $\hat{R}_{\mathbf{o}'}$ of the target range $R_{\mathbf{o}'}$ by solving the optimization problem (89).
15: Compute the phase estimates $(\hat{\phi}_l^{(\mathrm{TX})}, \hat{\phi}_m^{(\mathrm{RX})})$ and the frequency estimates $(\hat{f}_l^{(\mathrm{TX})}, \hat{f}_m^{(\mathrm{RX})})$ on the basis of (44)-(47) for any l and m.

Note also that, since $\lambda/4$ is usually small (0.975 mm in the radar system described in Section V), the position of the radar has to be precisely controlled; in practice, this result can be achieved by changing its position through a stepper motor, electronically controlled by a computer. Finally, it is worth pointing out that:

a) If a 2D virtual array is employed, a similar approach can be followed. However, the MIMO radar needs to be mechanically moved across a plane, like in the SAR system implemented in [4]. Therefore, in that case, the implementation of MBC becomes more complicated.

b) The procedure described above for FF-MBC is also exploited as it is in NF-MBC for setting up a synthetic aperture.

V. EXPERIMENTAL SETUP AND NUMERICAL RESULTS

In this section, we first illustrate the main technical features of the radar device employed in our experimental activities and describe the experimental setup developed for its calibration in far-field and near-field conditions. Then, we analyse some numerical results obtained through the FF-MBC, NF-MBC

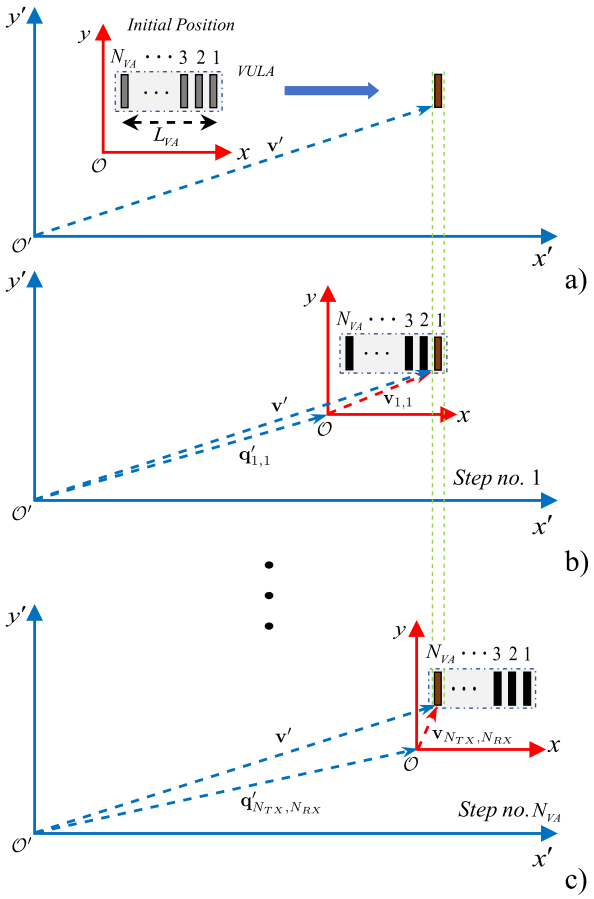

FIGURE 2. Representation of the procedure accomplished in FF-MBC for measurement acquisition: a) a reference point, identified by the vector $\mathbf{v}'$ with respect to the reference system $\mathcal{O}'$, is fixed before starting the acquisition procedure and the radar is moved from left to right in order to position its rightmost VA at the reference point itself; b) the first measurement is acquired through the rightmost VA (whose position is identified by the vector $\mathbf{v}_{1,1}$ with respect to the reference system $\mathcal{O}$); c) the last measurement is acquired through the leftmost VA of the array (the position of this VA is identified by the vector $\mathbf{v}_{N_T,N_R}$ with respect to the reference system $\mathcal{O}$).

and TC methods. Finally, we show the impact of calibration on SAR imaging.

A. EMPLOYED RADAR DEVICE

Our experimental work has aimed at calibrating the FMCW TIDEP-01012 Cascade mmWave radar (see Fig. 3-a), which is designed and manufactured by *Texas Instruments Inc* [28]. Its main parameters are: a) chirp slope $\mu = 87$ MHz/μs; b) central frequency $f_c = 77$ GHz (wavelength $\lambda = 3.89$ mm); c) sampling frequency $f_s = 10$ MHz; d) number of samples per chirp $N = 512$; e) chirp duration $T = 51$ μs. Moreover, this device is endowed with a planar array made of $N_T = 12$ TX and $N_R = 16$ RX antennas, so that the total number of available VAs is $12 \times 16 = 192$; however, only 9 TX antennas are used in our work, since a uniform linear portion of the whole virtual array is exploited. A representation of the physical TX and RX arrays, together with the employed VULA, is provided in Fig. 3b. The considered VULA has the following features:

1) It consists of $9 \times 16 = 144$ elements, but some of them are overlapped (see Fig. 3b). In practice, the overall number of *distinct* virtual elements is equal to 86.
2) The spacing of its adjacent virtual elements is $d_a = \lambda/4$.

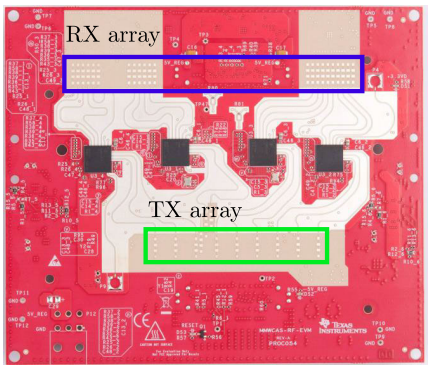

(a) The employed radar device.

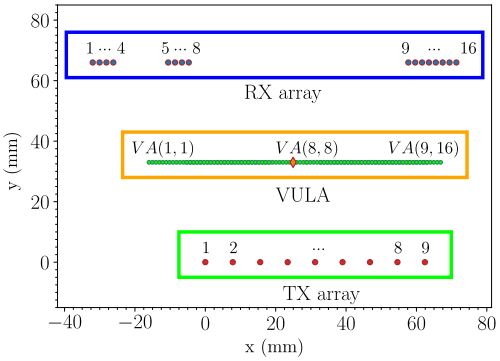

(b) Physical and virtual elements representation; only active elements are shown.

FIGURE 3. Representation of: a) the TI FMCW radar employed in our experiments (the physical TX and RX arrays are delimited by the green and blue rectangles, respectively); b) the configuration of the VULA considered in our work.

B. EXPERIMENTAL SETUP FOR TRADITIONAL AND MOVEMENT-BASED CALIBRATION METHODS

In our work, all the measurements required for TC have been acquired in a static outdoor environment and, in particular, in the garden of the Department of Engineering "Enzo Ferrari" (University of Modena and Reggio Emilia, Italy). The radar has been positioned on a table and a corner cube, having all its sides equal to 16 cm, has been put in front of it on a tripod, at a distance equal to 6.8 m (see Fig. 4), so that the far-field condition (31) is satisfied; moreover, electromagnetic absorbers have been placed on the tripod in order to mitigate its impact on calibration. Our measurements have been acquired through the 144 VAs contributing to the VULA.

On the other hand, all the measurements required for MBC have been acquired according to the procedure illustrated in Subsection IV-C for a VULA. For this reason, the radar has

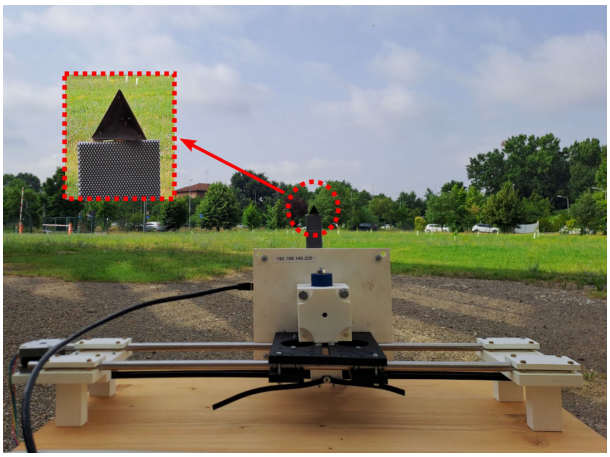

FIGURE 4. Experimental setup developed for the TC of a TIDEP-01012 Cascade mmWave radar. The rail on which the radar is mounted is not used in this scenario, i.e. the radar is kept in a *fixed* position. A corner cube, located in front of it, is installed on a tripod, whose legs are covered by electromagnetic absorbers in order to prevent stray reflections.

been installed on the mechanical horizontal rail[19] shown in Fig. 5. In both NF- and FF-MBC, 144 distinct measurements have been acquired; however, because of the presence of overlapped elements in the considered VULA, 86 different steps were needed to cover the whole virtual array itself[20] (see Fig. 2). As far as the targets are concerned, no explicit reference target is actually needed for FF-MBC; in fact, any target detectable in the surrounding propagation environment is useful for calibration purposes. For this reason, our radar device has been installed on a support and the required measurements have been acquired in the garden surrounding the Department of Engineering "Enzo Ferrari". In this case, all the electromagnetic echoes originate from multiple targets (all in far-field); in particular, in our experiments, the main echoes are generated by a near building and a fence at about 8 m from the radar, as shown in Fig. 5a. Near-field MBC, instead, has required the use of a reference target and, in particular, of a metal cylinder,[21] whose radius and height are equal to 5 and 15 cm, respectively; the overall experimental setup is shown in Fig. 5b. Note that:

a) The reference target is not required to be positioned exactly in front of the radar and that, in principle, prior knowledge of its position is not required. In practice, in our experiments, an approximate knowledge of its 2D position

(a) Setup for far-field MBC.

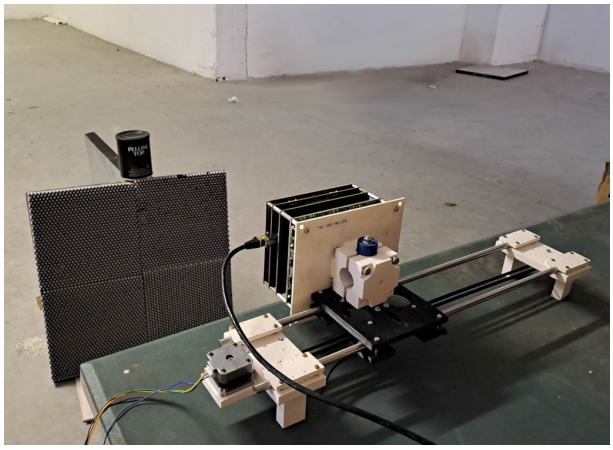

(b) Setup for near-field MBC.

FIGURE 5. Experimental setup developed for the NF- and FF-MBC of a TIDEP-01012 Cascade mmWave radar. In both cases, the radar device is moved along an horizontal rail by a stepper motor controlled through a portable computer. Note that, in far-field conditions, the main targets are a fence and the wall of a building. In near-field conditions, instead, a cylinder positioned on the top of a support (covered by electromagnetic absorbers) is used as pointwise target.

was available;[22] this simplifies solving the optimization problem (89) by narrowing the search space.

b) All the measurements have been acquired in a large (and almost empty) room, namely in the attic of one of the buildings of the Department of Engineering "Enzo Ferrari"; no anechoic chamber has been employed.

C. EXPERIMENTAL RESULTS FOR THE NEAR-FIELD AND FAR-FIELD SCENARIO

In this section, various numerical results, obtained for the TC, FF-MBC and NF-MBC of the radar device described in Subsection V-A, are analysed. In generating these results, the following choices have been made for the considered calibration methods:

[19] The maximum displacement allowed by this rail is equal to 30 cm; however, it has not been fully exploited since the total span required is given by the distance of the two farthest virtual elements (such a distance is denoted L_{VA} in Fig. 2), which is equal to 83,85 mm.

[20] In this case, the step size characterizing radar movements is equal to $\lambda/4 \simeq 0.975$ mm.

[21] Note that a cylinder represents a better approximation of a pointwise target than a corner cube; however, it can be used in near-field conditions only, since, having a small *radar cross section*, it may not be easily detectable in far-field conditions.

[22] The actual position of this target with respect to $\mathcal{O}'$ is $\mathbf{o}' = (-0.15, 0, 1)$ m, whereas the one provided by the estimation strategy described at the end of Subsection IV-B is $\hat{\mathbf{o}}' = (-0.15, 0, 0.99)$ m.

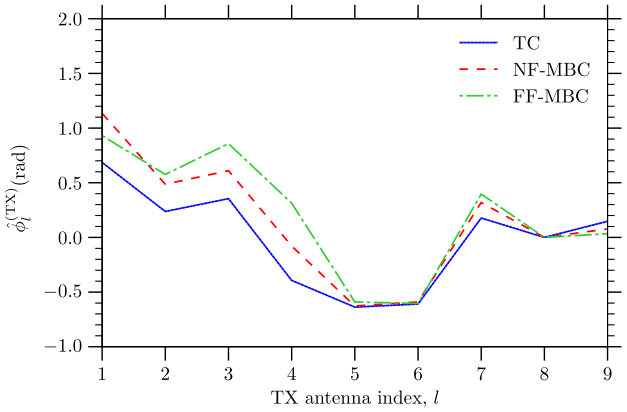

(a) Representation of the phases $\{\hat{\phi}_l^{(\mathrm{TX})}\}$; an array of 9 TX antennas is considered.

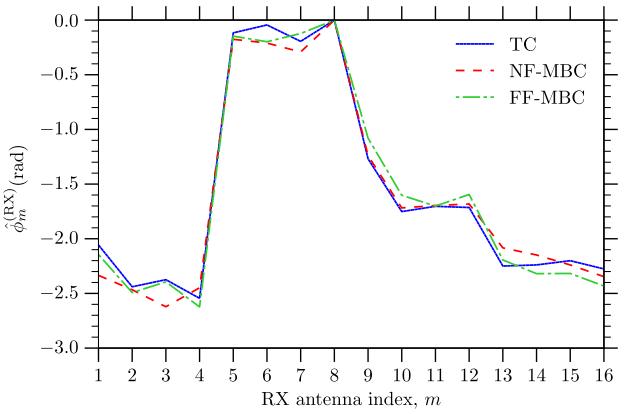

(b) Representation of the phases $\{\hat{\phi}_m^{(\mathrm{RX})}\}$; an array of 16 RX antennas is considered.

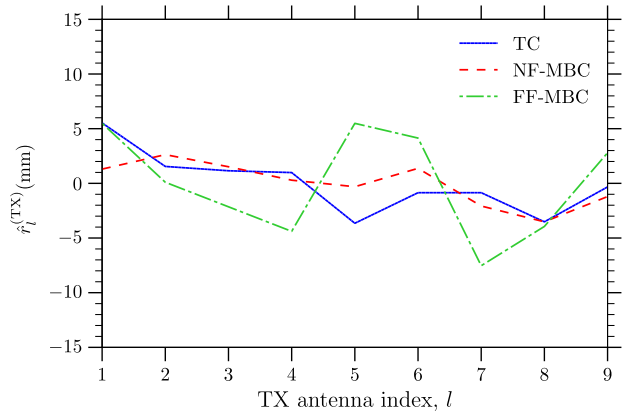

(c) Representation of the range biases $\{r_l^{(\mathrm{TX})}\}$; an array of 9 TX antennas is considered.

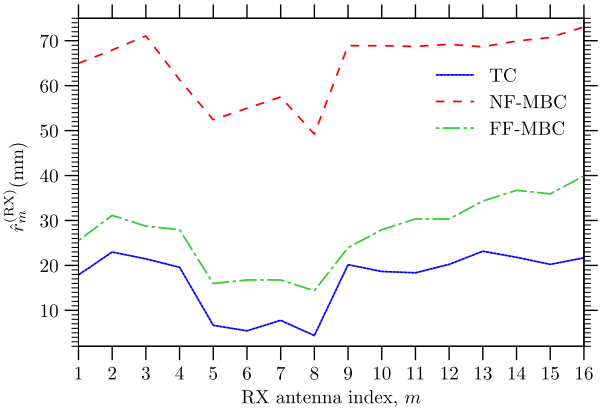

(d) Representation of the range biases $\{r_m^{(\mathrm{RX})}\}$; an array of 16 RX antennas is considered.

FIGURE 6. Representation of the phase biases ((a), (b)) and range biases ((c), (d)) evaluated for the TX and RX arrays associated with the selected VULA. Three different calibration methods are considered.

TC - The *complex single frequency estimation and cancellation* (CSFEC) algorithm developed in [29] has been used for estimating the frequency and the complex amplitude (and, consequently, the phase) of the complex tone associated with the employed reference target in place of the periodogram method; this choice has allowed us to achieve a better accuracy. Moreover, the following parameters have been selected for the CSFEC: 1) FFT order $N_0 = 8192$ (corresponding to an oversampling factor L equal to 16, since $N = 512$); 2) number of iterations $N_{it} = 8$.

FF-MBC - The order $N_0 = 6144$ has been selected in the evaluation of the FFT (68) (corresponding to an oversampling factor L equal to 12).

NF-MBC - Due to the lack of vertical movement in the employed rail, the elevation $\psi_{o'}$ of the reference target has not been estimated and has been assumed to be equal to zero. Accurate estimation of the target azimuth $\theta_{o'}$, instead, has been made possible by the synthetic aperture generated through the horizontal movement of the couple of TX and RX antennas associated with the VA $(8, 8)$ (i.e., with the central virtual element shown in Fig. 3b); in fact, this has made available $N_m = 86$ equally spaced channels, characterized by an inter-channel distance equal to $\lambda/4 = 0.975$ mm. The order $N_0^{(R)} = 1024$ ($N_0^{(\theta)} = 256$) has been adopted in the FFT processing applied to the measurements provided by the synthetic aperture in order to achieve range (azimuth) estimation. Moreover, similarly as TC, the CSFEC algorithm has been used, in place of the method described by (38), (40) and (41), to estimate the frequency and the complex amplitude (and, consequently, the phase) of the complex tone associated with the employed reference target; the values of the parameters selected for this algorithm are the same as those adopted in case of TC. The measurements acquired through the experimental setups illustrated in Figs. 4 and 5 have been processed to generate, for the set of TX and RX antennas associated with the considered VULA and for each of the calibration methods, the following quantities: a) the sets of frequency estimates $\{\hat{f}_l^{(\mathrm{TX})}\}$ and $\{\hat{f}_m^{(\mathrm{RX})}\}$ (see (44) and (46), respectively); the sets of phase estimates[23] $\{\hat{\phi}_l^{(\mathrm{TX})}\}$

[23]To ease the interpretation of our results, the mean value has been computed for each set and been subtracted from its elements, before representing them. Do not forget that, as already explianed in Section II, introducing the same phase shift on all the antennas does not have any effect on radar imaging algorithms.

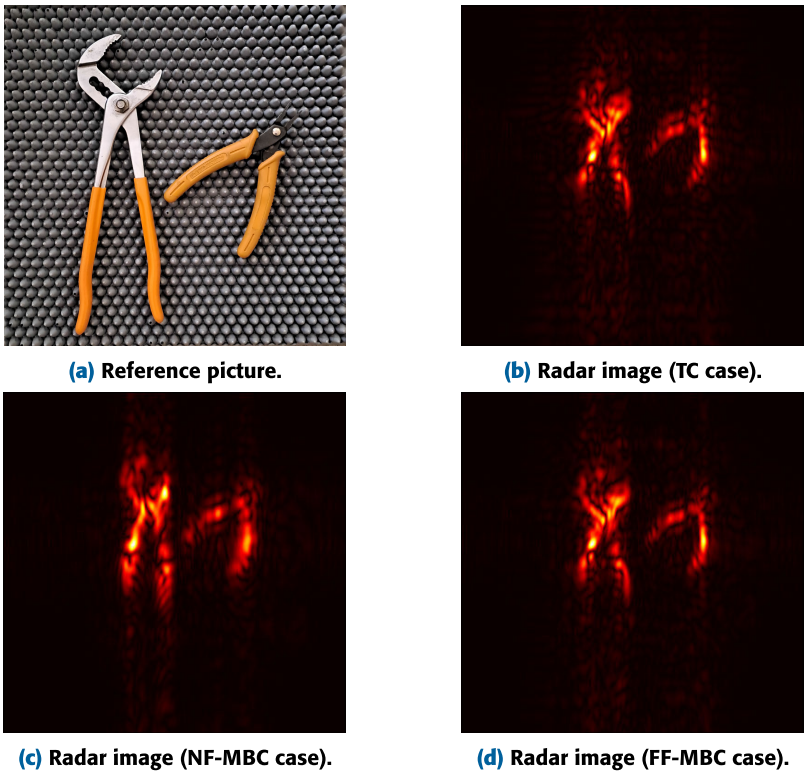

(a) Reference picture. **(b)** Radar image (TC case). **(c)** Radar image (NF-MBC case). **(d)** Radar image (FF-MBC case).

FIGURE 7. Reconstruction of a specific image (a) through the BPA. Three different methods are used for the computation of the calibration matrices: (b) TC; (c) NF-MBC; d) FF-MBC.

and $\{\hat{\phi}_l^{(\mathrm{RX})}\}$ (see (45) and (47), respectively). Then, these sets have been exploited to evaluate: a) the phase biases $\{\phi_l^{(\mathrm{TX})}\}$ and $\{\phi_m^{(\mathrm{RX})}\}$ shown in Figs. 6a and 6b, respectively; b) the range biases $\{r_l^{(\mathrm{TX})}\}$ and $\{r_m^{(\mathrm{RX})}\}$, shown in Figs. 6c and 6d. These results show that the phase and range biases evaluated through the three different calibration methods are similar. However, as it can be easily inferred from Fig. 6d, such methods behave differently with respect to the absolute phase bias. In fact, we have that:

a) The FF-MBC method, because of its nature, is unable to estimate the absolute range bias. Note that, if all the VAs were affected by same range bias, the estimates of the quantities $r_l^{(\mathrm{TX})}$ and $r_m^{(\mathrm{RX})}$ (28) would be equal to 0 for any l and m. This is due to the fact the FF-MBC method is only capable of detecting the *differences* among the range biases affecting distinct virtual elements.

b) In principle, the TC method would be able to estimate the absolute range bias if the reference target range R (30) was known with high accuracy. For instance, in our case, acquiring an accurate knowledge of R would require to estimate a distance of approximately 7 m with an accuracy in the order of a few centimeters;[24] this is not easy to do in practice. For this reason, in practice, a null range bias is assigned to a given reference antenna and all the other range biases are evaluated with respect to that antenna.

c) The NF-MBC method allows to estimate the absolute range bias. In fact, solving the optimization problem in (89) produces an accurate estimate of the *actual* position of the reference target (including its range) with respect to the reference system $\mathcal{O}$ *without* the need of evaluating $f_{l,m}^{(\mathrm{B})}$ (17). Moreover, in our experiments, since the reference target adopted for NF-MBC was close to the radar, it was easy to measure its distance with sufficient accuracy and validate the effectiveness of target range estimation through (89). In this case, since we were able to reliably estimate the reference target position, the absolute range bias can be trivially assessed by evaluating (78) and (29).

The considerations illustrated above explain why, in our numerical results, the range biases provided by NF-MBC are substantially different from the ones obtained through TC and FF-MBC (see Fig. 6d). However, apart from a constant offset, the range bias estimates $\{\hat{r}_l^{(\mathrm{TX})}\}$ evaluated through TC, FF-MBC and NF-MBC methods are similar.

Then, in order to assess the effectiveness of MBC, we exploited the obtained calibration matrices in the generation of a specific radar image through a well known MIMO-SAR algorithm, namely the *back projection algorithm* (BPA) [4]. This choice is motivated by the fact that BPA is very sensitive to phase mismatches, since these may appreciably affect the quality of the radar images it

[24]The exact distance between the radar and the reference target (i.e., the employed corner cube) was equal to 6.8 meters.

generates [31], [32], [33]. In our experimental set-up, the radar device has been rotated by 90 degrees with respect to our previous set-ups in order to generate, through its movement along the rail, a *uniform rectangular array* of size 86×300. The results we obtained in this case are shown in Fig. 7. More specifically, the reference image and the radar images generated by means of the BPA on the basis of our three different calibration matrices are shown in Fig. 7a, and in Figs. 7b, 7c and 7d,, respectively. The two objects appearing in the reference image are perfectly visible in all the radar images, which have similar quality. This result was expected, because the phases $\{\hat{\phi}_l^{(\mathrm{TX})}\}$ and $\{\hat{\phi}_m^{(\mathrm{RX})}\}$ (and, to a lesser extent, the frequencies $\{\hat{f}_l^{(\mathrm{TX})}\}$ and $\{\hat{f}_m^{(\mathrm{RX})}\}$ are similar, as shown in Fig. 6. The aim of this comparison is to show that three completely different approaches to calibration lead to the same result in terms of image quality, eve if they require different efforts to perform the calibration itself. It is also worth stressing that, while TC requires a pointwise target *and* a wide multipath-free area, NF-MBC only need a pointwise target and a *small* area (in this experiment, a free surface of about 1 m^2 in front of the radar was sufficient to obtain a good calibration) and FF-MBC does not pose *any* constraint on the surrounding propagation environment.

Our final results, shown in Fig. 8, concern the *beampatterns* observed for one and two corner cubes placed in front of the radar at a distance equal to 6.8 m (Fig. 8a) and 9.7 m (Fig. 8b), respectively. The interest in these results is motivated by the fact that they allow to quantify the impact of calibration accuracy on radar imaging. In fact, if a good calibration matrix is employed to compensate for frequency and complex amplitude mismatches in the TX and RX arrays, the angular profile observed in the presence of a pointwise target should exhibit a narrow main lobe and a low *side-lobe level* (SLL). In this case, a Kaiser-Bessel windowing function with $\alpha = 9$ [34] has been applied to the measurements, acquired through the considered VULA. Then, the resulting data have undergone 2D FFT processing for range and azimuth estimation (the orders $N_0^{(R)} = 2048$ and $N_0^{(\theta)} = 512$ have been selected for range and azimuth, respectively). Our results evidence that:

a) The FF-MBC method and, especially, the NF-MBC method offer the best results in terms of SLL in different scenarios.

b) In the considered case, despite all the efforts we made in the implementation of the TC approach (that should represent the golden standard in radar calibration), that method failed achieving the same performance as MBC in terms of SLL. This is due to the fact that, in practice, the implementation of TC is not easy.

Based on these results, we can conclude that the MBC methods perform better, thanks to their implementation simplicity (a low cost mechanical device for moving the radar horizontally has been employed in our laboratory). The FF-MBC method, in particular, does not even require any specific reference target to be placed in the field of view of the radar; this feature contributes to substantially reduce the effort required to perform phase and frequency calibration. The NF-MBC method, instead, requires a single pointwise target, but it can be placed anywhere in the proximity of the radar, with little or no control of its position (which can be accurately estimated through the procedure described in Section IV-B); once again, this substantially simplifies the calibration procedure.

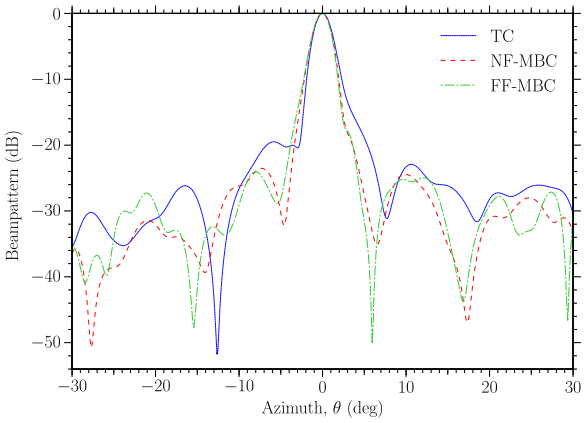

(a) Single corner cube ($R = 6.8$ m).

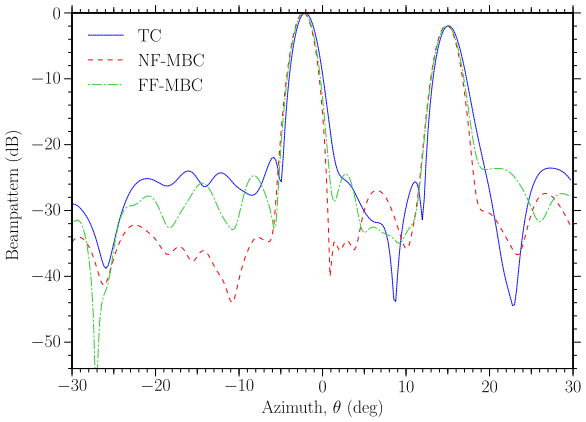

(b) Two corner cubes ($R = 9.7$ m).

FIGURE 8. Beampattern powers obtained for a) one corner cube anf b) two corner cubes placed in front of the considered radar device. Distinct curves refer to different choices for the calibration matrices.

VI. CONCLUSION

In this manuscript, two novel methods for the calibration of colocated MIMO radars have been proposed. They lend themselves to a simple implementation, since they do not require a controlled environment for the acquisition of the required measurements. Our numerical results have evidenced that, when applied to a commercial radar device, they are able to accurately estimate the phase and frequency mismatches in its TX and RX arrays; moreover, they outperform a calibration method commonly adopted in the technical literature. In this work we have only focused on phase and frequency mismatches across antennas. Our future

work aims at investigating other nonidealities of MIMO radars (with a particular interest in radar systems employing cascaded-chip devices), and at developing novel techniques to estimate and compensate for them.

REFERENCES

[1] S. M. Patole, M. Torlak, D. Wang, and M. Ali, "Automotive radars: A review of signal processing techniques," *IEEE Signal Process. Mag.*, vol. 34, no. 2, pp. 22–35, Mar. 2017.

[2] J. Hasch, E. Topak, R. Schnabel, T. Zwick, R. Weigel, and C. Waldschmidt, "Millimeter-wave technology for automotive radar sensors in the 77 GHz frequency band," *IEEE Trans. Microw. Theory Techn.*, vol. 60, no. 3, pp. 845–860, Mar. 2012.

[3] P. Stoica, J. Li, and Y. Xie, "On probing signal design for MIMO radar," *IEEE Trans. Signal Process.*, vol. 55, no. 8, pp. 4151–4161, Aug. 2007.

[4] M. E. Yanik, D. Wang, and M. Torlak, "Development and demonstration of MIMO-SAR mmWave imaging testbeds," *IEEE Access*, vol. 8, pp. 126019–126038, 2020.

[5] Y. Rockah and P. Schultheiss, "Array shape calibration using sources in unknown locations—Part I: Far-field sources," *IEEE Trans. Acoust., Speech, Signal Process.*, vol. ASSP-35, no. 3, pp. 286–299, Mar. 1987.

[6] Y. Rockah and P. Schultheiss, "Array shape calibration using sources in unknown locations—Part II: Near-field sources and estimator implementation," *IEEE Trans. Acoust., Speech, Signal Process.*, vol. ASSP-35, no. 6, pp. 724–735, Jun. 1987.

[7] A. J. Weiss and B. Friedlander, "Array shape calibration using sources in unknown locations—A maximum likelihood approach," *IEEE Trans. Acoust., Speech, Signal Process.*, vol. 37, no. 12, pp. 1958–1966, Dec. 1989.

[8] C. M. Schmid, C. Pfeffer, R. Feger, and A. Stelzer, "An FMCW MIMO radar calibration and mutual coupling compensation approach," in *Proc. EuRAD*, Oct. 2013, pp. 13–16.

[9] N. Petrov and A. Yarovoy, "Least squares calibration of MIMO radars with collocated arrays," in *Proc. 18th EuRAD*, Apr. 2022, pp. 213–216.

[10] A. Dürr, D. Schwarz, F. Roos, P. Hügler, S. Bucher, P. Grüner, and C. Waldschmidt, "On the calibration of mm-wave MIMO radars using sparse antenna arrays for DoA estimation," in *Proc. 16th EuRAD*, Oct. 2019, pp. 349–352.

[11] A. Dürr, B. Schneele, D. Schwarz, and C. Waldschmidt, "Range-angle coupling and near-field effects of very large arrays in mm-wave imaging radars," *IEEE Trans. Microw. Theory Techn.*, vol. 69, no. 1, pp. 262–270, Jan. 2021.

[12] J. Geiss, E. Sippel, M. Hehn, and M. Vossiek, "Antenna array calibration using a sparse scene," *IEEE Open J. Antennas Propag.*, vol. 2, pp. 349–361, 2021.

[13] F. Belfiori, W. van Rossum, and P. Hoogeboom, "Array calibration technique for a coherent MIMO radar," in *Proc. 13th IRS*, May 2012, pp. 122–125.

[14] W. Tian, Y. Li, C. Hu, Y. Li, J. Wang, and T. Zeng, "Vibration measurement method for artificial structure based on MIMO imaging radar," *IEEE Trans. Aerosp. Electron. Syst.*, vol. 56, no. 1, pp. 748–760, Feb. 2020.

[15] B. P. Ng, J. P. Lie, M. H. Er, and A. Feng, "A practical simple geometry and gain/phase calibration technique for antenna array processing," *IEEE Trans. Antennas Propag.*, vol. 57, no. 7, pp. 1963–1972, Jul. 2009.

[16] C. Vasanelli, F. Roos, A. Durr, J. Schlichenmaier, P. Hugler, B. Meinecke, M. Steiner, and C. Waldschmidt, "Calibration and direction-of-arrival estimation of millimeter-wave radars: A practical introduction," *IEEE Antennas Propag. Mag.*, vol. 62, no. 6, pp. 34–45, Dec. 2020.

[17] J.-W. Ting, D. Oloumi, and K. Rambabu, "FMCW SAR system for near-distance imaging applications—Practical considerations and calibrations," *IEEE Trans. Microw. Theory Techn.*, vol. 66, no. 1, pp. 450–461, Jan. 2018.

[18] J. Guetlein, A. Kirschner, and J. Detlefsen, "Calibration strategy for a TDM FMCW MIMO radar system," in *Proc. IEEE COMCAS*, Oct. 2013, pp. 1–5.

[19] M. Z. Ikram, M. Ali, and D. Wang, "Joint antenna-array calibration and direction of arrival estimation for automotive radars," in *Proc. IEEE RadarConf*, May 2016, pp. 1–5.

[20] S. Sadat, C. Ghobadi, and J. Nourinia, "Mutual coupling compensation in small phased array antennas," in *Proc. IEEE Antennas Propag. Soc. Symp.*, vol. 4, Jun. 2004, pp. 4128–4131.

[21] A. Lemma, E. Deprettere, and A.-J. van der Veen, "Experimental analysis of antenna coupling for high-resolution DOA estimation algorithms," in *Proc. 2nd SPAWC*, 1999, pp. 362–365.

[22] N. Petrov, O. Krasnov, and A. G. Yarovoy, "Auto-calibration of automotive radars in operational mode using simultaneous localisation and mapping," *IEEE Trans. Veh. Technol.*, vol. 70, no. 3, pp. 2062–2075, Mar. 2021.

[23] A. Figueroa, N. Joram, and F. Ellinger, "Automatic delay and phase mismatch calibration in FMCW MIMO radar," in *Proc. 17th EuRAD*, Jan. 2021, pp. 402–405.

[24] H. M. Aumann, A. J. Fenn, and F. G. Willwerth, "Phased array antenna calibration and pattern prediction using mutual coupling measurements," *IEEE Trans. Antennas Propag.*, vol. 37, no. 7, pp. 844–850, Jul. 1989.

[25] X. Tian, Q. Guo, T. Chang, and H.-L. Cui, "Phase self-calibration for millimeter wave MIMO imaging," in *Proc. 43rd Int. Conf. Infr., Millim., THz Waves (IRMMW-THz)*, Sep. 2018, pp. 1–2.

[26] B. J. Doring, P. R. Looser, M. Jirousek, and M. Schwerdt, "Reference target correction based on point-target SAR simulation," *IEEE Trans. Geosci. Remote Sens.*, vol. 50, no. 3, pp. 951–959, Mar. 2012.

[27] P. Heidenreich, A. M. Zoubir, and M. Rubsamen, "Joint 2-D DOA estimation and phase calibration for uniform rectangular arrays," *IEEE Trans. Signal Process.*, vol. 60, no. 9, pp. 4683–4693, Sep. 2012.

[28] Texas Instruments. (Jun. 2019). *Design Guide: TIDEP-01012; Imaging Radar Using Cascaded mmWave Sensor Reference Design*. [Online]. Available: https://www.ti.com/lit/ug/tiduen5a/tiduen5a.pdf

[29] P. D. Viesti, A. Davoli, G. Guerzoni, and G. M. Vitetta, "Recursive algorithms for the estimation of multiple superimposed undamped tones and their application to radar systems," *IEEE Trans. Aerosp. Electron. Syst.*, vol. 59, no. 2, pp. 1834–1853, Apr. 2023.

[30] J. Li and P. Stoica, *MIMO Radar Signal Processing*. Hoboken, NJ, USA: Wiley, 2008.

[31] T. Spreng, U. Prechtel, B. Schönlinner, V. Ziegler, A. Meusling, and U. Siart, "UWB near-field MIMO radar: Calibration, measurements and image reconstruction," in *Proc. EuRAD*, Oct. 2013, pp. 33–36.

[32] X. Zhuge and A. G. Yarovoy, "Three-dimensional near-field MIMO array imaging using range migration techniques," *IEEE Trans. Image Process.*, vol. 21, no. 6, pp. 3026–3033, Jun. 2012.

[33] Y. Liu, X. Xu, and G. Xu, "MIMO radar calibration and imagery for near-field scattering diagnosis," *IEEE Trans. Aerosp. Electron. Syst.*, vol. 54, no. 1, pp. 442–452, Feb. 2018.

[34] F. J. Harris, "On the use of windows for harmonic analysis with the discrete Fourier transform," *Proc. IEEE*, vol. 66, no. 1, pp. 51–83, Jan. 1978.

GIORGIO GUERZONI received the B.S. and M.S. degrees (cum laude) in electronics engineering and the Ph.D. degree in information and communication technologies from the University of Modena and Reggio Emilia, Italy, in 2019 and 2023, respectively. His research interests include signal processing and machine learning methods for MIMO radars.

ELAHE FAGHAND was born in Iran, in 1992. She received the B.S. degree from Shahed University, in 2015, and the M.S. degree in electrical engineering from Shahid Beheshti University, Tehran, Iran, in 2018, where she is currently pursuing the Ph.D. degree with the Department of Electrical Engineering. She is a Visiting Researcher with the Department of Engineering "Enzo Ferrari," University of Modena and Reggio Emilia, Modena, Italy. Her research interests include millimeter-wave radars, signal processing methods for MIMO radars, ultrawideband radar imaging systems, and the design of radio frequency circuits.

GIORGIO MATTEO VITETTA (Senior Member, IEEE) received the Dr.Ing. (cum laude) and Ph.D. degrees in electronic engineering from the University of Pisa, Italy, in 1990 and 1994, respectively. He has been a Full Professor of telecommunications with the University of Modena and Reggio Emilia, since 2001. He has coauthored more than 100 papers published on international journals and on the proceedings of international conferences. He has coauthored the book *Wireless Communications: Algorithmic Techniques* (John Wiley, 2013). His main research interests include wireless and wired data communications, localization systems, MIMO radars, and smart grids. He has served as an Area Editor for IEEE TRANSACTIONS ON COMMUNICATIONS and as an Associate Editor for the IEEE WIRELESS COMMUNICATIONS LETTERS and IEEE TRANSACTIONS ON WIRELESS COMMUNICATIONS.

LORIS VINCENZI received the M.S. degree in civil engineering and the Ph.D. degree in structural mechanics from the University of Bologna, Italy, in 2003 and 2007, respectively. He is currently an Associate Professor of structural engineering with the University of Modena and Reggio Emilia. His research interests include the structural health monitoring of bridges and buildings, the experimental identification of dynamic properties of structures, the pedestrian induced vibrations on footbridges, and the structural model updating.

ESFANDIAR MEHRSHAHI received the B.Sc. degree in electrical engineering from the Iran University of Science and Technology, Tehran, Iran, in 1987, and the M.Sc. and Ph.D. degrees in electrical engineering from the Sharif University of Technology, Tehran, in 1991 and 1998, respectively. Since 1990, he has been involved in several research and engineering projects with the Iran Telecommunications Research Center (ITRC). He is currently an Associate Professor with Shahid Beheshti University (SBU), Tehran. His main research interests include the nonlinear simulation of microwave circuits, low-phase noise oscillators, and computational electromagnetics.

Open Access funding provided by 'Università degli Studi di Modena e Reggio Emilia' within the CRUI CARE Agreement